



Master's Thesis in Physics

Gain Characterisation of ANTARES PMTs for SWG0

Kavan Harshal Purohit

Supervisor: Dr Alison Mitchell

Erlangen Centre for Astroparticle Physics

Submission date: 23.10.2025

Abstract

This thesis investigates whether the photomultiplier tubes (PMTs) recovered from the ANTARES neutrino telescope can be reused in the Southern Wide-field Gamma-ray Observatory (SWGGO). To answer this, a simple but careful laboratory setup was built and used to record single-photoelectron (SPE) signals under stable, low light. From these data, the PMT gain was measured at several voltages and a standard power-law relation was calibrated. The nominal operating high voltage for each PMT was then derived for a target gain of 5×10^7 . The workflow was kept reproducible, with automated scripts for acquisition, fitting, and summary plots, so that the steps can be repeated, edited and checked in future.

It was found that most ANTARES PMTs reach the required gain at moderate voltages, typically around 1350–1500 V, which is compatible with SWGGO electronics and leaves comfortable operating headroom. The spread of gain–voltage slopes is compact, so calibration across many channels should be efficient. Overall, the results indicate that reuse of ANTARES PMTs is feasible and cost-effective, offering a fast and environmentally sustainable route to support SWGGO construction.

Contents

Abstract	I
Contents	II
1 Introduction	1
1.1 Motivation and Goals	1
1.2 Cosmic Rays and Gamma-Ray Astronomy	2
1.3 Southern Wide-field Gamma-ray Observatory (SWGGO)	5
1.3.1 Scientific Motivation and Objectives	5
1.3.2 Detector Concept and Design	6
1.3.3 Site and Development Timeline	8
1.4 ANTARES Neutrino Detector	9
1.4.1 Design and Configuration	9
1.4.2 Decommissioning and Legacy	11
2 Theoretical Background	13
2.1 Cosmic Rays and Extensive Air Showers	13
2.1.1 Particle Interactions and Shower Development	13
2.1.2 Electromagnetic and Hadronic Showers	15
2.2 Cherenkov Radiation	16
2.2.1 Physical Principles	17
2.2.2 Cherenkov Emission in Extensive Air Showers	18
2.3 Photomultiplier Tubes (PMTs)	19
2.3.1 Structure and Operational Principle	20
2.3.2 Characteristics and Important Parameters	22
2.3.3 ANTARES PMTs	26
3 Experimental Setup and Instrumentation	27
3.1 Measurement concept	27
3.2 Light-tight environment	27
3.3 Instruments and signal chain	29
3.3.1 High voltage.	29

3.3.2	PMT base and signal pick-off.	30
3.3.3	Light source and Pulse Generator	31
3.3.4	Oscilloscope	32
3.4	Acquisition settings and procedure	33
3.4.1	ANTARES optical-module extraction (context)	34
4	Data Analysis Methods	36
4.1	Overview of the workflow	36
4.2	Data structure and metadata	36
4.3	Preprocessing and charge definition	37
4.3.1	Voltage calibration and baseline.	37
4.3.2	Integration windows and charge proxy.	37
4.3.3	Robustness to window choice.	37
4.4	Charge spectrum and valley logic	38
4.5	Parametric response model and two-stage estimation	39
4.5.1	Model	39
4.5.2	Two-stage estimation and rationale.	39
4.6	Gain extraction and propagated uncertainties	40
4.7	Gain-voltage calibration and nominal operating voltage	41
4.8	Additional python scripts	42
5	Results	43
5.1	Overview of the Measurement Procedure	43
5.2	Gain measurements	45
5.2.1	ANTARES PMTs	45
5.2.2	Reference PMT and group comparison	51
5.3	Verdict on nominal HV of ANTARES PMTs	54
6	Conclusions	56
6.1	Summary of Aims and Approach	56
6.2	Result discussions	56
6.2.1	Fleet-level operating voltages and slopes	56
6.2.2	Reference cross-check	57
6.2.3	Data quality, uncertainties, and robustness	57
6.3	Implications for SWGO Reuse	57
6.4	Limitations of this thesis	58
6.5	Closing Statement	59
	Bibliography	60
A	Additional Data Tables	63

B Git repository for scripts	69
List of Figures	70
List of Tables	75
Declaration of Originality	76
Acknowledgments	77

1 Introduction

1.1 Motivation and Goals

“Our challenge to understand the universe often begins with the dimmest flicker of light — a photon that has travelled across the cosmic distances to tell its story.” The Southern Wide-field Gamma-ray Observatory (SWGGO) is one of the future ground-based gamma-ray detectors that are being developed to capture that story [3]. It follows the water-Cherenkov detection technique, which includes the production of Cherenkov light by secondary particles, generated from extensive air showers, which are detected by the photomultiplier tubes (PMTs) [3]. For the construction of such a detector, a few hundred to potentially a thousand PMTs are required, and hence, the cost and feasibility play a role in the development of such projects.

One of the favourable approaches to reduce both the cost and environmental impacts is to reuse the PMTs extracted from other decommissioned detectors. One such recently disassembled detector is the ANTARES neutrino telescope, which served its purposes for almost two decades in the Mediterranean Sea [3]. It offered a significant stock of functional PMTs, whose performance has yet to be systematically evaluated before they can be reused for SWGGO. Hence, each of these PMTs must be tested to determine their usability, which includes computing the electrical characteristics, such as achievable gain and stability under high voltage, which can satisfy the requirements of SWGGO [3].

This thesis aims to investigate whether ANTARES PMTs can be reused for the construction of SWGGO by conducting a detailed gain characterisation, which will be compared to reference values of a new PMT. For this characterisation, a dedicated laboratory setup is established exclusively to acquire, process and analyse single photoelectron signals from ANTARES PMTs. This study

emphasises computing the gain as a function of applied high voltage (HV). The ultimate objective is to identify the operational HV range for which the used ANTARES PMTs can achieve values of gains compatible with SWGO's specifications.

1.2 Cosmic Rays and Gamma-Ray Astronomy

Cosmic rays are high-energy particles coming from space that continuously bombard the Earth's atmosphere. These were discovered by Victor Hess in 1912 through the famous balloon-borne experiments, which initiated the whole field of experimental astroparticle physics. Cosmic Rays are primarily consist of protons ($\sim 90\%$), alpha particles ($\sim 9\%$) and a small fraction of heavier nuclei and electrons. When these enters the Earth's atmosphere, they interact with atmospheric nuclei that creates cascades of secondary particles, known as extensive air showers (EAS) [9, 13].

The energy spectrum of cosmic rays, as seen in Figure 1.1, covers a vast range of more than twelve orders of magnitude, and across this range, the flux drops by roughly thirty orders of magnitude. It roughly follows a power law distribution, $\Phi(E) \propto E^{-\gamma}$, where the spectral indices slightly changes at two characteristic points known as 'knee' ($\sim 3 \times 10^{15}$ eV) and the 'ankle' ($\sim 10^{18}$ eV). These characteristics are associated with transitions between different acceleration mechanisms and possible source populations [9].

The primary particles collides with atmospheric nuclei while entering the atmosphere. This results into the formation of a cascade of secondary particles. Its electromagnetic component mainly arises from bremsstrahlung and pair production, whereas the hadronic component produces mesons which then decays into muons and neutrinos. When these processes combine, it leads to the formation of an EAS as shown in Figure 1.2. When such showers are detected and studied, we get information about the energy, direction, and identity of the primary particle [13].

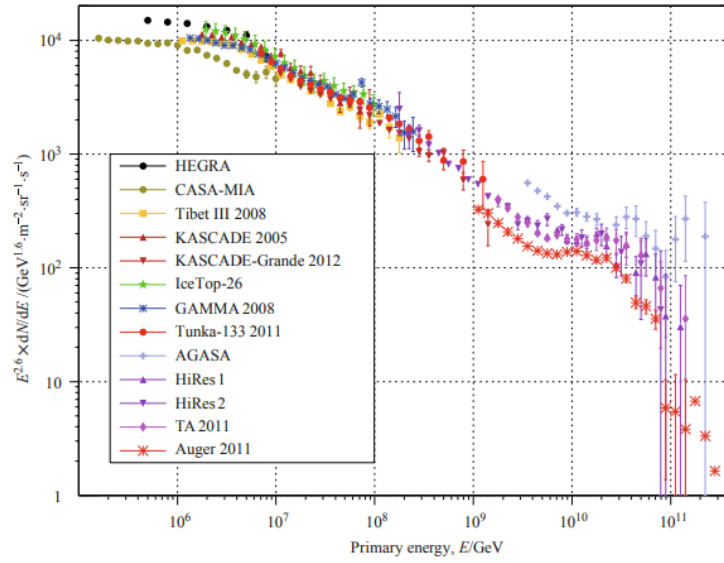


Figure 1.1: All-particle cosmic-ray energy spectrum compiled from multiple air-shower experiments, showing the characteristic features known as the “knee” and the “ankle”. Data from HEGRA, CASA-MIA, KASCADE, IceTop, Tunka, HiRes, Telescope Array, and Auger are shown for comparison. Adapted from Gaisser and Stanev [9].

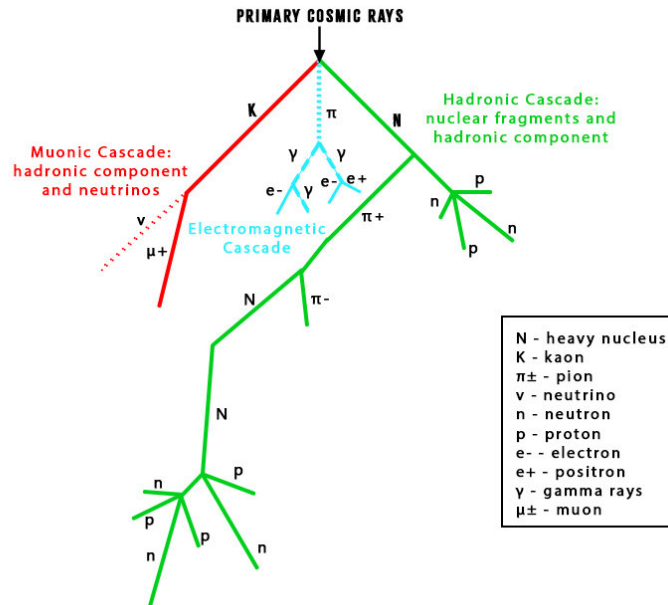


Figure 1.2: Schematic representation of an extensive air shower showing its hadronic, electromagnetic, and muonic components. Adapted from Pawlicki [23].

A particular subclass of cosmic radiation certainly includes high-energy gamma rays. Being electrically neutral, gamma rays propagate through interstellar magnetic fields without deflection. Consequently, they point back to their astrophysical source, and the astronomy of gamma rays is a direct probe of perhaps the most energetic processes in the universe. The processes which incorporate such energy will involve interactions in Supernova remnants, pulsar wind nebulae, Active Galactic Nuclei, and Gamma-Ray Bursts. Gamma rays result from inverse Compton scattering and neutral pion decay as an end product of proton-proton interactions [6].



Figure 1.3: Global distribution of major ground-based gamma-ray observatories. Current facilities are shown in green, planned or future observatories in blue, and past experiments in red. The planned SWGO site in South America will provide wide-field coverage of the southern sky. Figure adapted from [29]

The study of the gamma-ray sky is pursued with both space and ground-based observatories. While space missions like Fermi-LAT cover energies up to a few hundred GeV, ground-based detectors cover sensitivity into the TeV–PeV range by observing air-shower signatures. A World map of all past, current and future gamma-ray observatories is shown in fig 1.3. In these, the HAWC observatory and LHAASO have reported exceptional performances in the identification of TeV–PeV gamma-ray sources, including the discovery of so-called PeVatrons capable of accelerating beyond 10^{15} eV [2, 6]. Despite such great development, the southern sky remains largely unexplored. This gap

in observations basically justifies the construction of the SWGO that will be able to continuously provide a wide-field coverage of the southern hemisphere with unparalleled sensitivity [3].

1.3 Southern Wide-field Gamma-ray Observatory (SWGO)

The Southern Wide-field Gamma-ray Observatory (SWGO) is a next-generation ground-based experiment planned for the exploration of the high-energy gamma-ray sky of the Southern hemisphere. By its establishment, it addresses one of the most important observational gaps in gamma-ray astronomy: the absence of a wide-field, high-duty-cycle detector in the south that can continuously monitor the sky for sources up to the PeV range. While northern facilities like the HAWC and LHAASO have achieved remarkable discoveries, the inner regions of our Galaxy—that is, the Galactic Centre and much of the plane—remain inaccessible from their locations [3].

In Figure 1.3, it has been already shown that the majority of the existing or planned wide-field gamma-ray observatories are located in the Northern hemisphere. This geographical bias implies a poor coverage factor for transient sources and only moderate coverage factors for a proper study of extended structures such as the Fermi Bubbles and the central molecular zone. SWGO will overcome this limitation by providing full-time access to the Southern sky from a high-altitude site in South America.

1.3.1 Scientific Motivation and Objectives

SWGO is proposed to address a host of questions in high-energy astrophysics. For instance, the precise location of galactic accelerators (PeVatrons), the mechanism of propagation and diffuse emission of cosmic rays, and prospective new physics like dark matter signatures and Lorentz-invariance violation. This continuous all-sky monitor will further provide transient alerts and survey context to IACT arrays like CTAO [3].

The observable region of the sky from the SWGO site is displayed in Figure 1.4, showing the Galactic Plane in color and highlighting in grey those zones that fall outside the instrument’s field of view. This visualizes capability of SWGO to monitor the Galactic Centre region directly overhead, and allows deep observations of the most active regions in the Milky Way.

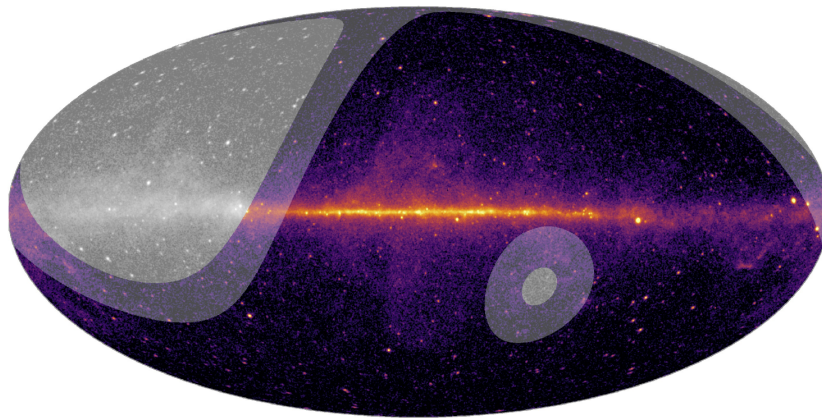


Figure 1.4: Sky visibility of the Southern Wide-field Gamma-ray Observatory (SWGO). The colored band represents the Galactic Plane and the regions visible to SWGO above 45° and 60° elevation from its planned southern-hemisphere site. Adapted from Abreu *et al.* [3].

1.3.2 Detector Concept and Design

SWGO will use the water-Cherenkov detector technique—common in principle to HAWC and LHAASO—but optimized for southern-sky coverage. Each detector unit is a container of water instrumented with two PMTs, one looking upwards and another one downwards, separated by a reflective Tyvek barrier. This dual-layer configuration increases muon tagging and gamma-hadron separation, hence increasing the background rejection.

A scheme of a single SWGO detector unit is shown in Figure 1.5. This dual-PMT configuration improves event reconstruction and enables efficient muon-tagging capability [18]. Thousands of detector units would comprise the array in a graded-density pattern with a compact, high-density central core

surrounded by regions of successively lower detector density—covering an effective area of approximately one square kilometer. This arrangement enables the effective detection in a huge energy range, from hundreds of GeV to several PeV in a very efficient way. Figure 1.6 gives the schematic drawing of the planned layout of the SWGO-A array consisting of seven detector clusters, each with 55 water-Cherenkov detectors (WCDs) with a central field node represented by the rectangle in blue. This modular, cluster-based structure not only simplifies calibration and maintenance but also allows for flexible expansion in array building during future stages of the observatory’s development [3].

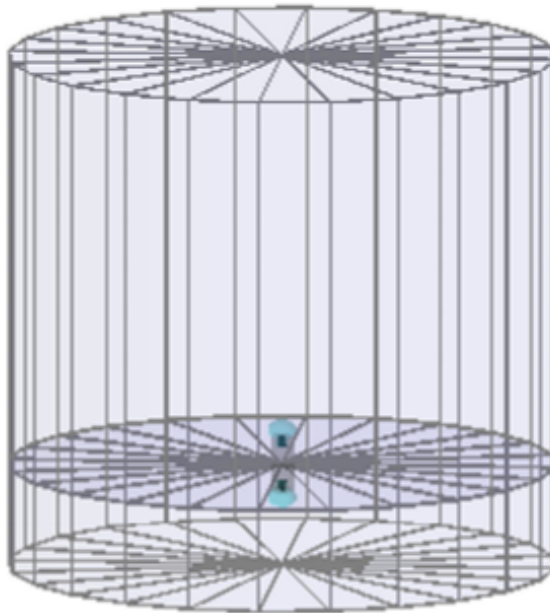


Figure 1.5: Schematic view of a water-Cherenkov detector (WCD) unit designed for the Southern Wide-field Gamma-ray Observatory (SWGO). The cylindrical tank contains two PMTs mounted vertically—one facing upward and one facing downward—to enable muon tagging and gamma-hadron discrimination. Adapted from Leitl [18].

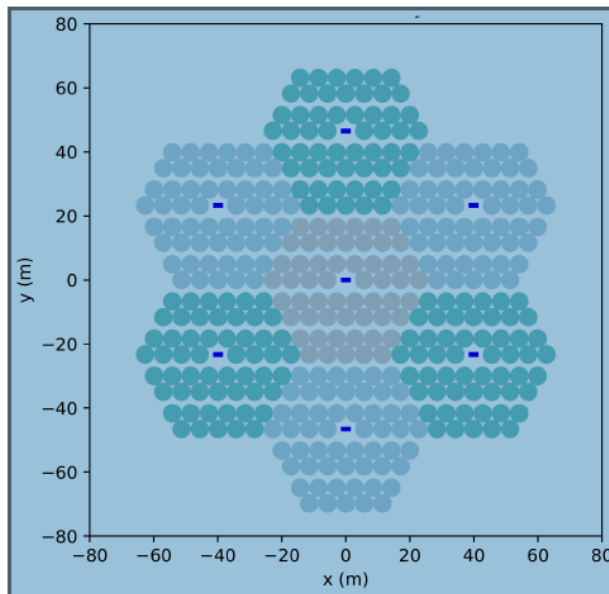


Figure 1.6: Planned SWGO-A layout showing seven detector clusters, each consisting of 55 water-Cherenkov detectors (WCDs) and a central field node (blue rectangle). This configuration forms the prototype subarray of the full SWGO design. Adapted from Abreu *et al.* [3].

1.3.3 Site and Development Timeline

The primary site selected for SWGO is the *Pampa La Bola*, part of the Atacama Astronomical Park in Northern Chile at 4,770 m a.s.l. It offers outstanding atmospheric transparency, very low humidity, proximity to major facilities like ALMA, and by its latitude, most Galactic Centre observations are close to the zenith as can be seen in Figure 1.4.

In this collaboration, the roadmap has been structured through the series of milestones summarized in Table 1.1. These milestones indicate progress that evolves from an initial R&D phase to a full-scale deployment with the construction of the first operational subarray—SWGO-A: the initial scientific phase of the observatory.

Milestone	Completed
M1 R&D Phase Plan Established	Q1 2020
M2 Science Benchmarks Defined	Q2 2020
M3 Reference Configuration & Options Defined	Q4 2020
M4 Site Shortlist Complete	Q3 2022
M5 Candidate Configurations Defined	Q1 2022
M6 Performance of Candidate Configurations Evaluated	Q3 2023
M7 Preferred Site Identified	Q2 2024
M8 Design Finalised	–
M9 Construction & Operation Proposal Complete	–

Table 1.1: Milestones of the SWGO R&D phase, together with completion dates for milestones already completed [3].

1.4 ANTARES Neutrino Detector

The ANTARES (Astronomy with a Neutrino Telescope and Abyss environmental RESearch) detector was a deep-sea neutrino telescope located in the Mediterranean Sea at about 40 km off shore from Toulon, France, built at a depth of about 2475 m. It was operated between 2008 and 2022, and it was the first underwater neutrino telescope that reached continuous long-term operation. It was designed to detect high-energy neutrinos coming from astrophysical sources by detecting the Cherenkov light emitted by the charged secondary particles produced in neutrino interactions within or around the instrumented water volume [11, 27].

1.4.1 Design and Configuration

ANTARES is made up of twelve flexible detection lines moored to the sea floor and held straight by buoys. Each line was equipped with 25 storeys, each hosting three optical modules (OMs) oriented 45° downwards to optimize the sensitivity for up-going neutrino-induced muons. Each optical module contained a 10-inch PMT enclosed within a 17-inch glass sphere together with the front-end electronics, power supply, and calibration components. The array therefore was made up of 885 PMTs in total [27].

The layout and geometry of ANTARES are sketched schematically in Figure 1.7. The lines were spaced about 70 m apart, covering a footprint of $\sim 0.1 \text{ km}^2$, while vertically the instrumented height was about 350 m. A separate instrumentation line provided environmental monitoring, calibration and acoustic positioning to counteract misalignment under sea currents.

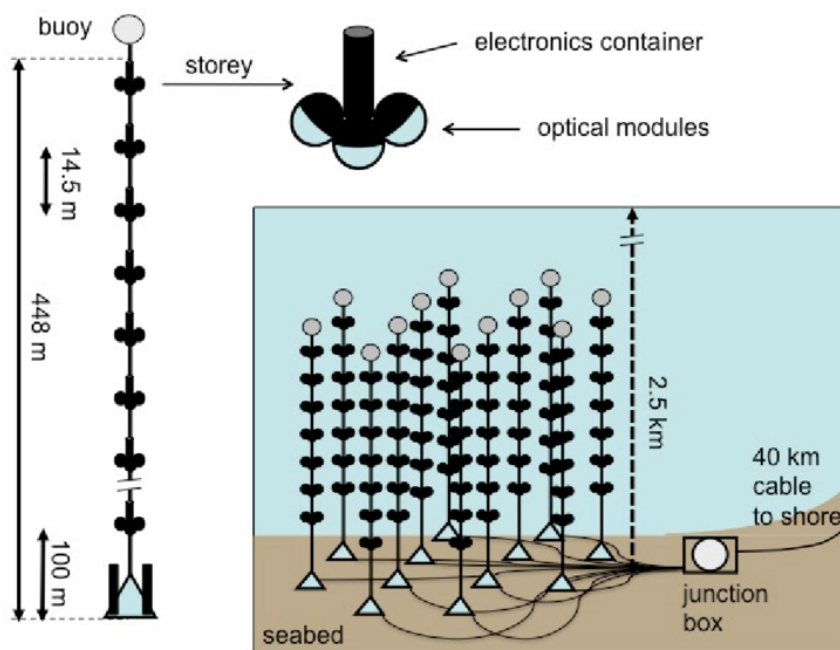


Figure 1.7: Schematic view of the ANTARES neutrino telescope in the Mediterranean Sea, showing the arrangement of the detection lines with storeys and optical modules, the sea-bed junction box, and the 40 km cable connecting the detector to the onshore station. Adapted from Zornoza and Zúñiga [7].

ANTARES was designed based on the observation of Cherenkov light emitted when relativistic charged particles, basically muons produced by neutrino interactions in seawater, are traversed by this medium. Such photons are focused by the PMTs, which transform them into electrical pulses. The times of arrival and the pulse amplitudes were measured with the purpose of reconstructing the trajectory and energy of the incoming neutrino.

The PMTs used in ANTARES, that is shown in Figure 1.8, were Hamamatsu R7081-20 PMTs, featuring a 10-inch hemispherical photocathode, a gain of

approximately 10^7 , and excellent single photoelectron timing resolution [22]. Their long-time reliability in such a hostile deep-sea environment already proved them as promising candidates to be reused in other large astroparticle experiments. For SWGO, these recovered ANTARES PMTs offer the possibility to evaluate the feasibility of sustainable detector construction while reducing costs and material waste. Therefore, it is relevant that this work tries to decide whether these refurbished PMTs can still provide adequate gain stability and linearity after so many years of operation.

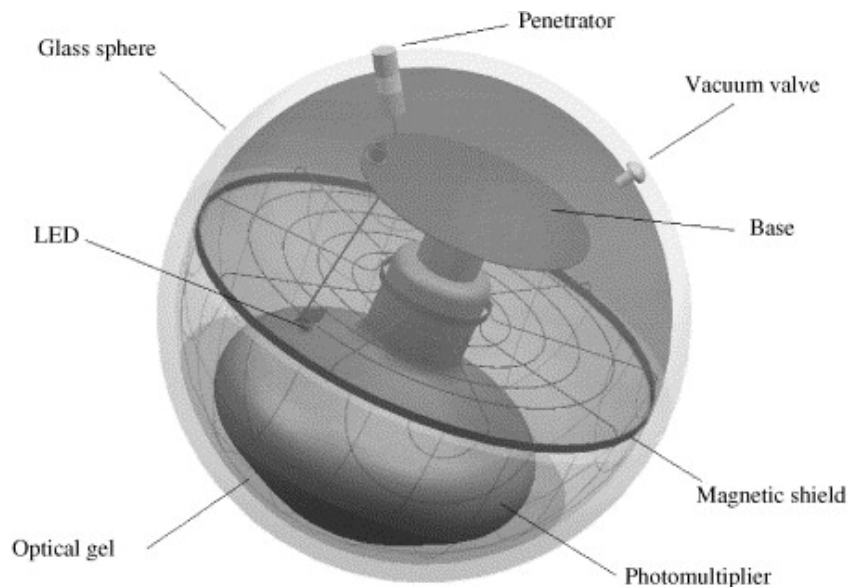


Figure 1.8: Schematic view of a single ANTARES optical module (OM), showing the internal components including the 10-inch Hamamatsu R7081-20 PMT, optical gel, magnetic shield, LED calibration device, and the pressure-resistant glass sphere. Adapted from Zornoza and Zúñiga [7].

1.4.2 Decommissioning and Legacy

After over a decade of operation, ANTARES was shut off in 2022, allowing for the deployment of its successor, KM3NeT—a fully new-generation Mediterranean neutrino telescope with larger instrumented volume and angular resolution [28]. During this decommissioning, thousands of optical modules were recovered and will be preserved for possible reuse in future projects. Those recovered PMTs, after being refurbished and characterized, may extend their

scientific contribution within SWGO by offering an innovative case of sustainable hardware re-deployment in astroparticle physics.

In this thesis, the gain characterization of these extracted ANTARES PMTs forms the bedrock for their suitability studies for inclusion in the SWGO detector array.

2 Theoretical Background

While the previous chapter introduced the motivation and experimental context, this chapter provides the physical principles underlying the detection of cosmic rays and the measurement of PMT response.

2.1 Cosmic Rays and Extensive Air Showers

As discussed earlier, cosmic rays are high-energy charged particles that originate from extraterrestrial sources, the energy range starting from approximately 10^9 eV to over 10^{20} eV. While they reach Earth, an accelerator laboratory forms, and hence high-energy interaction studies which are beyond the reaches of far terrestrial accelerators are enabled. Cosmic rays are mainly protons and helium nuclei, and heavier ions, but a small part are electrons and positrons. Their differential flux of primary cosmic rays follows the steep power-law distribution,

$$\Phi(E) \propto E^{-\gamma}, \quad (2.1)$$

where $\Phi(E)$ denotes the number of particles per unit energy, area, time, and solid angle; E is the particle energy, and γ is the spectral index that characterizes the slope of the spectrum, with spectral indices of $\gamma \approx 2.7$ below the knee and $\gamma \approx 3.1$ above the knee [9, 5].

2.1.1 Particle Interactions and Shower Development

An energetic primary while entering the atmosphere interacts with air nuclei, mostly nitrogen and oxygen, at a height of around 15–25 km. Highly abundant

secondary mesons are produced from the first hadronic collision, dominated by pions and kaons. These secondaries further interact and decay to give rise to an EAS.

Longitudinal development of the shower may be crudely approximated by the Heitler – Matthews model, in which the cascade is treated as a series of particle multiplications until the average energy per secondary falls below a critical energy E_c . As a function of depth t in radiation lengths, the total number of particles in the electromagnetic component may be expressed as,

$$N_{\max} \approx \frac{E_0}{E_c}, \quad (2.2)$$

where E_0 is the primary energy. For air, $E_c \approx 85$ MeV for electrons and positrons. The depth of the shower maximum, X_{\max} , scales logarithmically with the primary energy and depends on the mass of the primary particle, providing a handle for composition studies [20].

The schematic representations in Figure 2.1 illustrate the basic structure of (a) electromagnetic and (b) hadronic cascades as described by the Heitler–Matthews model, emphasizing the multiplicative branching of particles through bremsstrahlung, pair production, and pion decay.

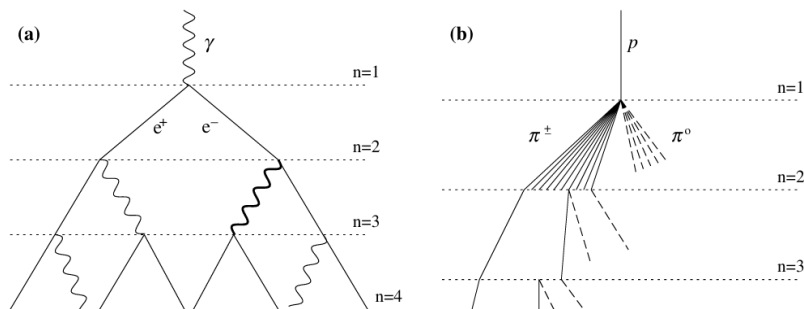


Figure 2.1: Schematic views of (a) an electromagnetic cascade and (b) a hadronic shower. In the hadronic cascade, dashed lines indicate neutral pions that decay rapidly into photons, generating electromagnetic sub-showers. The diagrams illustrate the multiplicative nature of shower development as described by the Heitler–Matthews model. Adapted from Matthews [20].

2.1.2 Electromagnetic and Hadronic Showers

The electromagnetic (EM) component of an EAS arises from the decay of neutral pions, $\pi^0 \rightarrow 2\gamma$, whose photons initiate cascades through pair production and bremsstrahlung,

$$\gamma \rightarrow e^+ + e^-, \quad e^\pm \rightarrow e^\pm + \gamma. \quad (2.3)$$

This process continues, until the energies of the secondary particles drop below E_c — or exactly where ionization losses become dominant. The charged pions and kaons initiate a good hadronic component which maintains the cascade through successive interactions and decays like $\pi^\pm \rightarrow \mu^\pm + \nu_\mu(\bar{\nu}_\mu)$. Muons thus produced are relatively long-lived, reach the ground, and turn out to be a very good tracer for the hadronic content of the shower [15].

This same balance between the electromagnetic and hadronic processes determines not only the particle composition of an air shower but also its longitudinal development. The most important observable characterizing this evolution is the depth of the shower maximum, X_{\max} , which defines the point at which the atmospheric depth attains its maximum value: As can be seen in Figure 2.2, lighter primaries like protons produce showers that are developing deeper in the atmosphere, while heavier nuclei, such as iron, interact earlier, producing shallower cascades. The separation of these X_{\max} distributions across energies provides an essential diagnostic for the inference of the primary mass composition of cosmic rays [15, 1].

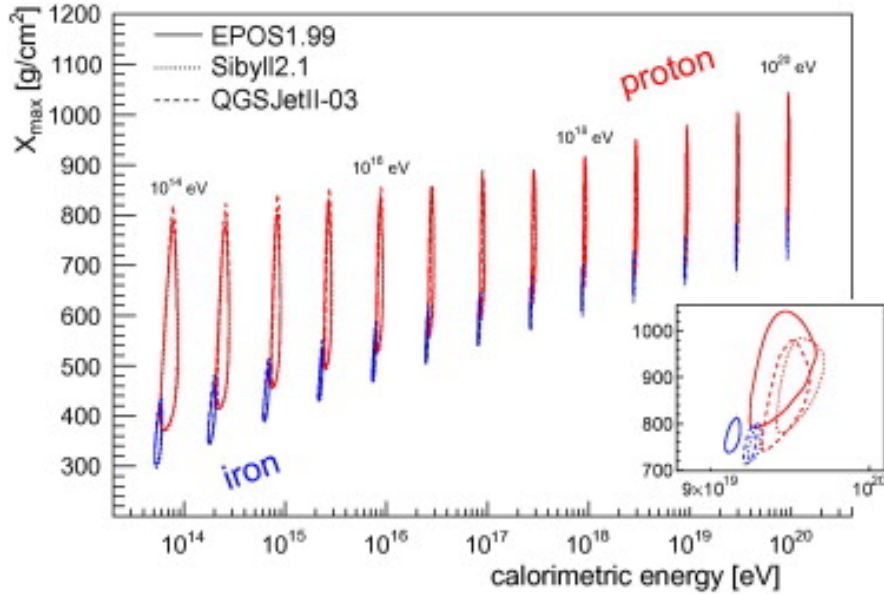


Figure 2.2: Simulated depth of shower maximum X_{\max} versus calorimetric energy E_{cal} for proton (red) and iron (blue) primaries using three hadronic-interaction models: EPOS 1.99, Sibyll 2.1, and QGSJetII-03. The separation of the distributions illustrates the sensitivity of X_{\max} to the primary mass and to the relative contributions of electromagnetic and hadronic components in shower development. Adapted from Kampert and Unger [15].

2.2 Cherenkov Radiation

Charged particles travelling through a dielectric medium at velocities exceeding the phase velocity of light in that medium emit electromagnetic radiation known as *Cherenkov radiation*. This effect, discovered experimentally by Pavel Cherenkov in 1934 and theoretically described by Tamm and Frank in 1937, forms the fundamental detection principle for many astroparticle experiments including HAWC, LHAASO, and SWGO. In extensive air showers, relativistic electrons, positrons, and muons produce Cherenkov photons both in the atmosphere and within the water of detector tanks, where they are subsequently detected by photomultiplier tubes (PMTs) [8, 12, 9].

2.2.1 Physical Principles

When a charged particle is passing in a medium of refractive index n at a velocity $v = \beta c$ larger than the phase velocity of light (c/n) of the light wave in that medium, its electromagnetic field distorts to induce coherent polarization along its path. The polarized atoms relax by emitting light along a cone wavefront, similar to a sonic boom generated by a supersonic object. Thus, the condition for Cherenkov emission is given by,

$$\beta n > 1, \quad (2.4)$$

or equivalently,

$$\cos \theta_c = \frac{1}{\beta n}, \quad (2.5)$$

where θ_c is the Cherenkov angle between the particle trajectory and the emitted light [8, 12].

For ultrarelativistic particles ($\beta \approx 1$), the Cherenkov angle in water ($n \approx 1.33$) is approximately 41° , while in air at sea level ($n \approx 1.0003$) it is about 1.3° . The number of photons emitted per unit path length and per unit wavelength interval is given by the Frank–Tamm formula:

$$\frac{d^2 N}{dx d\lambda} = \frac{2\pi\alpha}{\lambda^2} \left(1 - \frac{1}{\beta^2 n^2(\lambda)} \right), \quad (2.6)$$

where α is the fine-structure constant and λ is the wavelength of emitted light [8]. Equation 2.6 shows that the photon yield increases strongly towards shorter wavelengths, which explains the bluish colour of Cherenkov radiation.

Figure 2.3 illustrates the emission geometry of Cherenkov light produced by a relativistic charged particle traversing a medium.

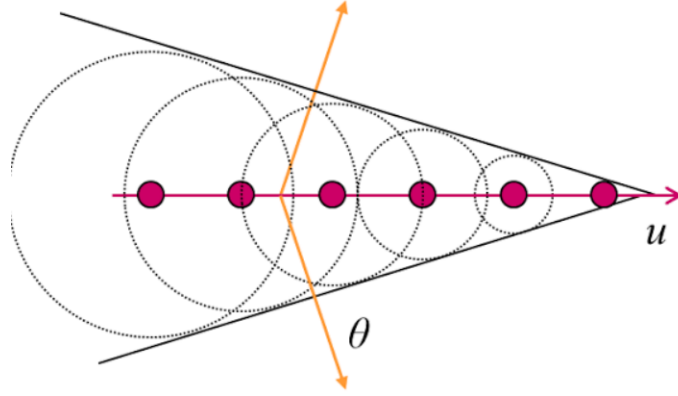


Figure 2.3: Schematic representation of Cherenkov radiation showing the characteristic light cone emitted by a charged particle moving faster than the phase velocity of light in a dielectric medium. The opening angle θ_c satisfies $\cos \theta_c = 1/(\beta n)$. Adapted from Alaeian [4].

2.2.2 Cherenkov Emission in Extensive Air Showers

In the context of cosmic-ray and gamma-ray detection, the Cherenkov light is produced both in the atmosphere and in the water-Cherenkov detectors employed at ground. In air, the Cherenkov photons emitted by secondary electrons and positrons form large light pools of about 120 m radius on the ground. It can be recorded by IACTs. At ground level, the charged particles entering water produce additional Cherenkov light that is focused by submerged PMTs. In the amplitude and time structure of the Cherenkov signal, information on the amount, direction, and energy of the primary particles is included. Since the Cherenkov emission is prompt and directional, then this allows the precise reconstruction of the particle arrival times enabling the air-shower front reconstruction and the coincidence measurements between detectors. In large arrays, such as those considered for the SWGO, signals from water-Cherenkov detectors integrate to provide a continuous monitoring of extensive air showers with high duty cycle and wide field of view [3, 30].

Figure 2.4 illustrates how Cherenkov radiation produced by secondary charged particles is detected in a water-Cherenkov detector (WCD). As these relativistic particles traverse the water volume, they emit Cherenkov photons along a cone defined by the angle θ_c . The resulting light front propagates toward

the base of the tank, where PMTs record the arrival time and intensity of the signals. The geometry of the Cherenkov cone and the time distribution of detected photons are key observables for reconstructing the shower direction and for distinguishing gamma-induced events from hadronic backgrounds.

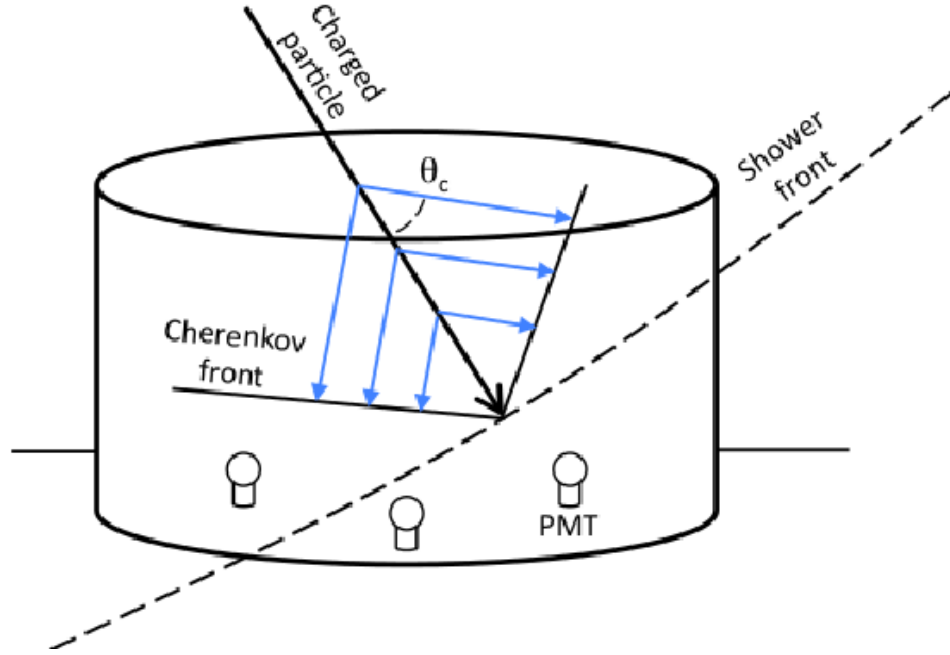


Figure 2.4: Schematic illustration of Cherenkov light production and detection in a water-Cherenkov detector (WCD). A relativistic charged particle from an extensive air shower passes through the water volume, emitting Cherenkov photons at an angle θ_c with respect to its trajectory. The light front reaches the PMTs mounted at the bottom, where the resulting photoelectrons are amplified to produce measurable signals. Adapted from Abreu *et al.* [3].

2.3 Photomultiplier Tubes (PMTs)

PMTs are very sensitive photon detectors, converting weak optical signals into proportionate electrical pulses of measurable strength. Since their discovery many decades ago, they have been playing a very important role in astroparticle and nuclear physics experiments. In fact, IceCube, HAWC, and

ANTARES provide just a few examples of observatories where PMTs are used as primary sensors. The detection concept for SWGO is based on an underwater-Cherenkov detector using PMTs, which will provide a readout of Cherenkov light produced by charged secondary particles crossing the water volume. Their high gain and nanosecond response and low noise make them peculiarly suitable to detect weak and fast optical signals [16, 19, 26].

2.3.1 Structure and Operational Principle

A PMT is an evacuated glass tube comprising a photosensitive cathode, focusing electrodes, a cascade of secondary-emission dynodes, and a collecting anode. When photons strike the photocathode, they liberate electrons via the photoelectric effect. These photoelectrons are then accelerated and directed by focusing electrodes onto the first dynode, where each impact releases several secondary electrons. This process repeats across successive dynodes, producing an avalanche of electrons that are finally collected at the anode to yield a measurable current pulse [25, 17].

Figure 2.5 schematically illustrates the basic internal structure of a PMT. The multiplication mechanism relies on the principle of secondary electron emission, where the overall gain G is given by

$$G = \prod_{k=1}^N \alpha_k \delta_k, \quad (2.7)$$

with N being the number of dynodes, δ_k the secondary emission ratio of the k^{th} dynode, and α_k the collection efficiency between dynodes [17].

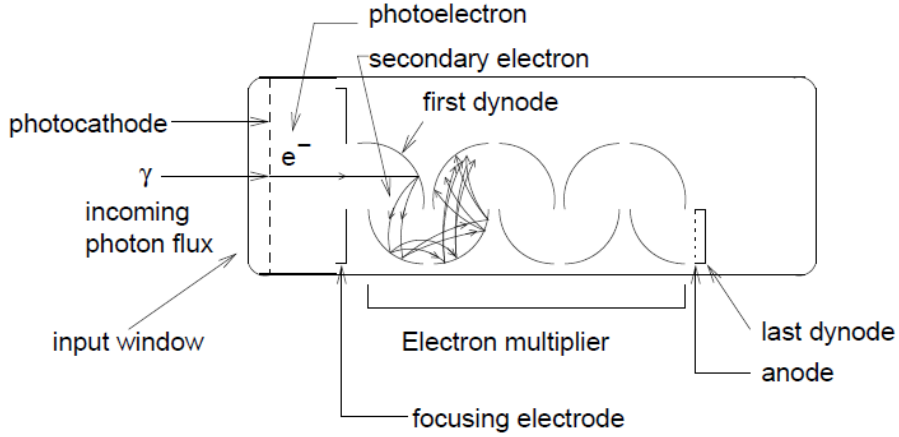


Figure 2.5: Schematic representation of a PMT showing the photocathode, focusing electrodes, dynode chain, and anode. Incident photons release photoelectrons at the photocathode, which are accelerated toward the first dynode, generating secondary electrons that are successively multiplied and collected at the anode. Adapted from Hamamatsu Photonics [24].

The photocathode, usually composed of alkali or bialkali compounds such as SbKCs, converts incident photons to electrons according to the relation

$$E = h\nu - \phi, \quad (2.8)$$

where E is the electron kinetic energy, $h\nu$ the photon energy, and ϕ the work function of the cathode material.

The probability that a photon produces an emitted electron defines the quantum efficiency (QE), which peaks around 420 nm for bialkali cathodes used in the R7081-20 PMTs [25, 17].

The voltage distribution across dynodes is maintained by a resistive divider network, typically integrated into the PMT base. Capacitors are often added across the final dynodes to stabilize potentials during large current pulses, ensuring a consistent gain and pulse linearity [17, 14]. A simplified electrical schematic of the base circuitry is shown in Figure 2.6.

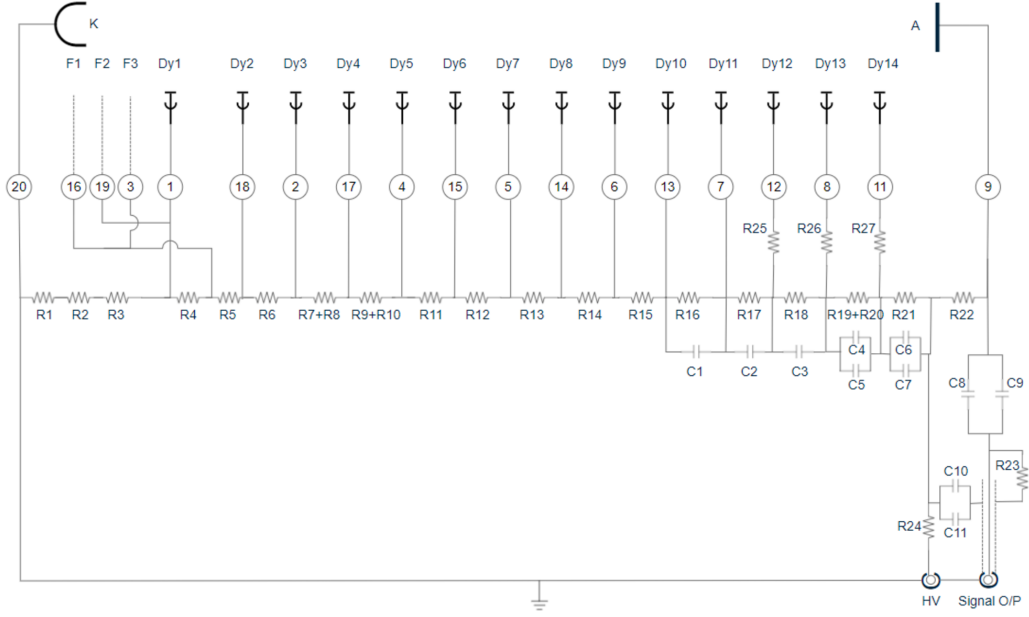


Figure 2.6: Simplified base-circuit schematic of the Hamamatsu R7081-20 PMT. The high-voltage divider network distributes the bias across 14 dynode stages and focusing electrodes, while capacitors stabilize the potential differences to ensure gain linearity and timing stability. The signal output is coupled capacitively to the readout electronics. Redrawn taking inspiration from [14, 17].

2.3.2 Characteristics and Important Parameters

The most relevant performance parameters for PMTs used in astroparticle physics include the gain, quantum efficiency, single-photoelectron (SPE) response, dark current, and transit-time spread (TTS). Their interplay determines the achievable energy and timing resolutions of Cherenkov detectors.

Gain

The gain measures the overall increase or multiplication in the number of electrons from the photocathode to the anode. It follows a power-law dependence on the applied high voltage,

$$G(V) = G_0 \left(\frac{V}{V_0} \right)^\kappa, \quad (2.9)$$

where $\kappa \approx 6\text{--}10$ depends on the dynode material, dynode count and secondary-emission properties. [26, 25]. For the Hamamatsu R7081-20, a gain of 10^7 is typically achieved at 1.7–2.0 kV [25].

Figure 2.7 illustrates an example of the gain–voltage relationship for one of the tested ANTARES PMTs (ID: ST5498), showing a logarithmic fit to the measured data.

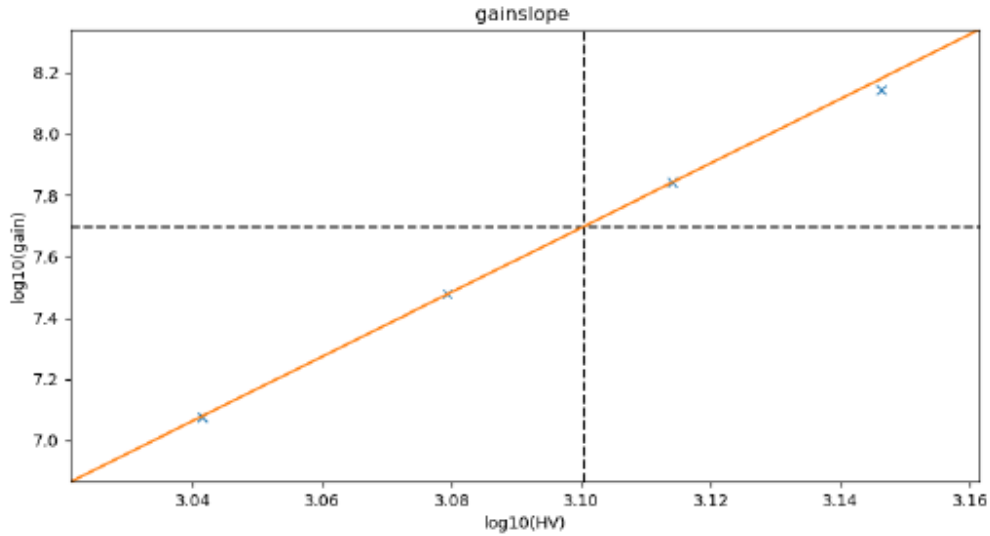


Figure 2.7: Measured gain–voltage relation for the ANTARES PMT ST5498. The logarithmic fit illustrates the expected power-law dependence, $G \propto V^\kappa$, where κ is obtained from the slope of the fitted line. In this case, the value of $\kappa \approx 8.5$

Single Photoelectron (SPE) Response

The response to a single photoelectron is characterized by the charge distribution of the output pulse. The peak-to-valley (P/V) ratio measures the separation between the single-photoelectron peak and the noise pedestal, which provides a measure of signal quality. A clear separation of this SPE peak is shown in Figure 2.8, within the SPE charge spectrum. For the R7081-20, a typical P/V ratio is about 2.5 [25]. This parameter is crucial for precise gain calibration and for distinguishing real photon events from dark noise.

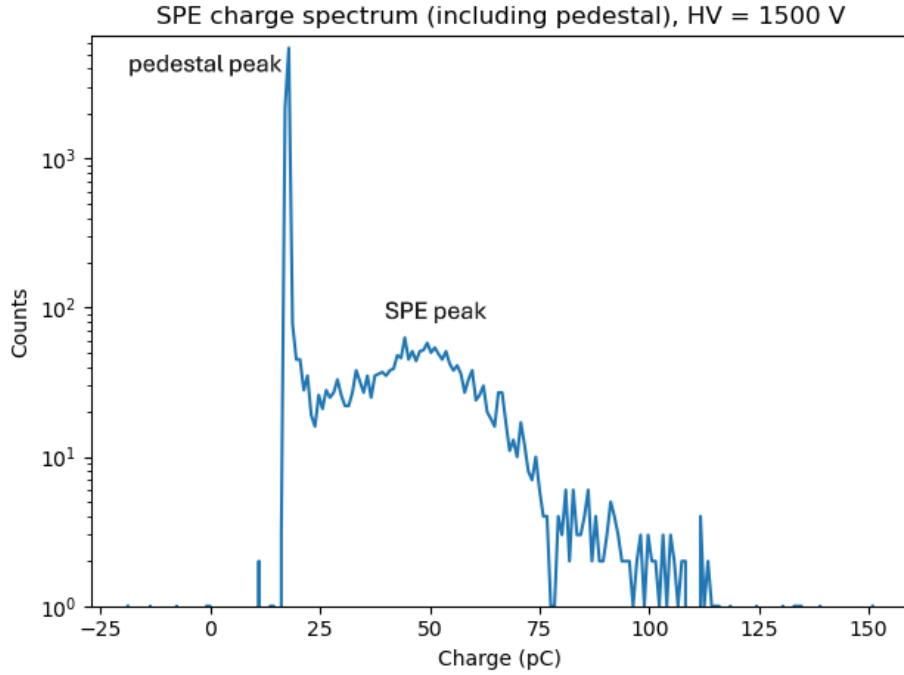


Figure 2.8: Single-photoelectron charge spectrum with a clearly separated SPE peak.

Dark Current and Noise

Even in the absence of light, thermionic emission, leakage currents, and radioactive impurities can produce spurious signals known as dark counts. For large-area bialkali PMTs like the R7081-20, the dark count rate ranges between 9 and 19 kHz after 15 hours in darkness at room temperature [25]. A stable dark current level below $5 \mu\text{A}$ is required for low-noise operation in Cherenkov detectors [17].

Timing Characteristics

Timing precision in PMTs is governed by the electron transit time and its spread (TTS), which determines how accurately photon arrival times can be measured. For the R7081-20, the mean transit time is approximately 78 ns with a TTS of 3.3 ns [25]. Such timing stability ensures nanosecond-level coincidence precision across multiple detector modules, a prerequisite for reconstructing shower directions in ANTARES and SWGO [22].

Quantum Efficiency

The quantum efficiency (QE) of a PMT represents the probability that an incident photon striking the photocathode will release a photoelectron. It is defined as

$$QE = \frac{N_e}{N_\gamma}, \quad (2.10)$$

where N_e is the number of emitted photoelectrons and N_γ is the number of incident photons. The QE depends strongly on the photocathode material and the wavelength of the incoming light, typically peaking in the blue–ultraviolet region for bialkali cathodes used in the Hamamatsu R7081–20 PMTs [25, 19].

In the case of Cherenkov detectors, where the light spectrum is concentrated in the near–UV to blue range, an even high QE in the same region is required to maximize photon detection efficiency. Shown in Figure 2.9 is a typical QE curve for a bialkali photocathode, which peaks at about 25–30% around 400 nm.

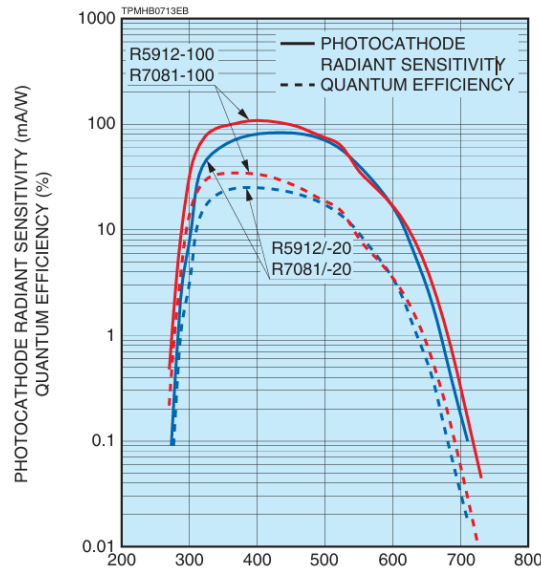


Figure 2.9: Quantum efficiency and photocathode radiant sensitivity of the Hamamatsu R7081-20 PMT as a function of wavelength. The bialkali photocathode exhibits peak sensitivity in the blue region near 400 nm. Adapted from Hamamatsu Photonics [10].

2.3.3 ANTARES PMTs

The ANTARES detector used the Hamamatsu R7081-20 PMT, a 10-inch hemispherical head-on type, developed for deep-sea operations at depths of up to 2500 m. It features a 14-stage box-and-line dynode structure as earlier shown in Figure 2.6, which balances large collection area at the first dynode with uniform focusing through later stages [17]. The PMT's borosilicate-glass window allows wavelengths above 300 nm, with maximum sensitivity around 420 nm, which matching the Cherenkov spectrum in water. Table 2.1 summarizes its key specifications.

Table 2.1: Main parameters of the Hamamatsu R7081-20 PMT [25, 22, 17].

Parameter	Typical Value	Unit
Photocathode material	Bialkali (SbKCs)	–
Spectral response range	300–650	nm
Peak wavelength	420	nm
Quantum efficiency at 390 nm	25	%
Dynode structure	Box-and-Line, 14 stages	–
Applied voltage for $G = 10^7$	1700–2000	V
Transit time / spread	78 / 3.3	ns
P/V ratio (SPE)	2.5	–
Dark count rate (15 h dark)	9–19	kHz
Weight	1.15	kg

In this thesis, a new R7081-20 PMT (SR:TM0007) is used to compare the testing results of the ANTARES PMTs.

3 Experimental Setup and Instrumentation

3.1 Measurement concept

To determine the gain–voltage relation as shown in Figure 2.7, of 10” ANTARES PMTs, the photocathode is illuminated with short laser pulses at fixed geometry and recording the anode response as waveforms for single–photoelectron (SPE) analysis. A Rigol DG1022 waveform generator gates an Alphalas PLDD-50MHV pulsed laser driver and simultaneously provides a hardware trigger to a Tektronix MSO54 oscilloscope. The oscilloscope acquires at **6.25 GS/s** with a **200 ns** acquisition window (**20 ns/div**). The PMT is mounted in a custom cradle, and the light is delivered via a fibre cable pointed at the photocathode; the source to PMT distance is kept constant for the whole run. The PMT base divider used here is the same design as shown in Figure 2.6 (anode readout with 50Ω).

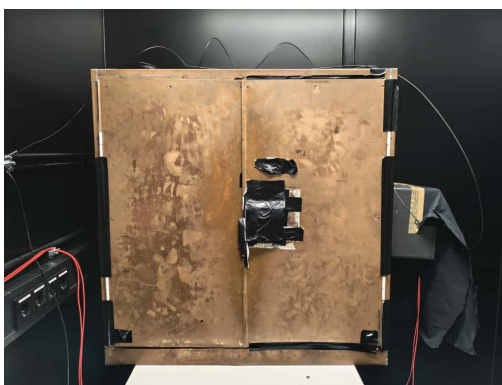
3.2 Light-tight environment

All measurements are performed inside a dedicated dark room as shown in Figure 3.1. Remaining door gaps were taped and filled alongwith the tiniest gaps and the door stayed locked during data taking with dark room lights off.



Figure 3.1: Dark room with the light-tight measurement box. Cables are routed via feedthroughs.

Power strips and signal/HV cables are routed along the walls and into a light-tight dark box as shown in Figure 3.2a. The box provides light-proof feedthroughs, matte black interior, and a small fiber mount that fixes the laser position with respect to the photocathode which is shown in Figure 3.2b. Before each session I performed a quick light-leak check (laser off, HV on) and confirmed a stable baseline.



(a) Dark box closed.



(b) Dark box open.

Figure 3.2: Light-tight measurement setup: (a) with the dark box closed and (b) with the dark box open, showing the PMT placed inside.

3.3 Instruments and signal chain

The instruments setup in the lab is shown in Figure 3.3.

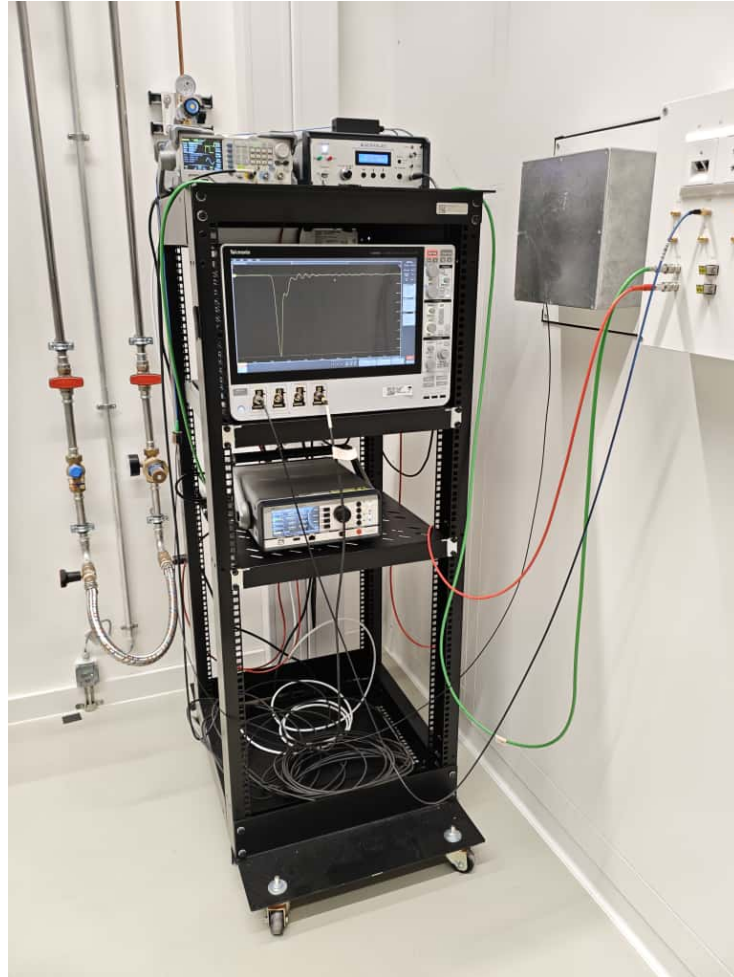


Figure 3.3: Whole instrument setup in the lab.

3.3.1 High voltage.

Bias is supplied by an iseg SHR high-voltage (HV) source, which is shown in 3.4. I used conservative ramping and current-limit settings and verified grounding before operation. HV and return (ground) are routed with shielded cables to the custom base.



Figure 3.4: iseg SHR high-voltage supply used for PMT biasing.

3.3.2 PMT base and signal pick-off.

Both the divider base (Figure 3.5b) and the signal pick-off (Figure 3.5a) enclosure were manufactured in the FAU Physics Department Mechanical Workshop. The pick-off provides AC-coupled anode output to the scope with 50 Ω termination. Short, impedance-matched coax cables are used throughout to avoid reflections.



(a) Signal pick-off device



(b) 14 pin adapter

Figure 3.5: (a) Signal pick-off device for HV and signal routing, and (b) 14-pin socket adapter interfacing the 10" PMT.

3.3.3 Light source and Pulse Generator

The light source is gated by an Alphas Laser PLDD-50MHV driver which is shown in Figure 3.6. Light is delivered as free fiber to the photocathode (no diffuser). During all measurements the laser driver was operated in DDS mode at a fixed repetition rate of 100 kHz. The Rigol DG1022 produces a pulse gate at ~ 1 kHz with 50% duty and $1.0V_{pp}$, for the laser and a synchronous trigger for the scope. The channel that generates the pulse in pulse generator is synced by providing a manual delay of 140 ns from the generator settings itself. This is done to acquire the waveform in the Oscilloscope at a specific and correct position, ensuring uniformity across all measurements. The rep-rate and gate width were set such that the average occupancy stays in the SPE regime (verified in data).



Figure 3.6: Signal generation: Rigol DG1022 gating the Alphas PLDD-50MHV pulsed driver.

3.3.4 Oscilloscope

Data are recorded with a Tektronix MSO54 which is shown in Figure 3.7. The acquisition settings (synchronized to the DG1022 trigger) are:

- Sample rate $f_s = 6.25$ GS/s,
- Record length $T_{\text{rec}} = 200$ ns (20 ns/div),
- 50Ω input, vertical scale chosen to avoid saturation,
- FastFrame/sequence mode for efficient bursts,
- Sample size $N = 10,000$.

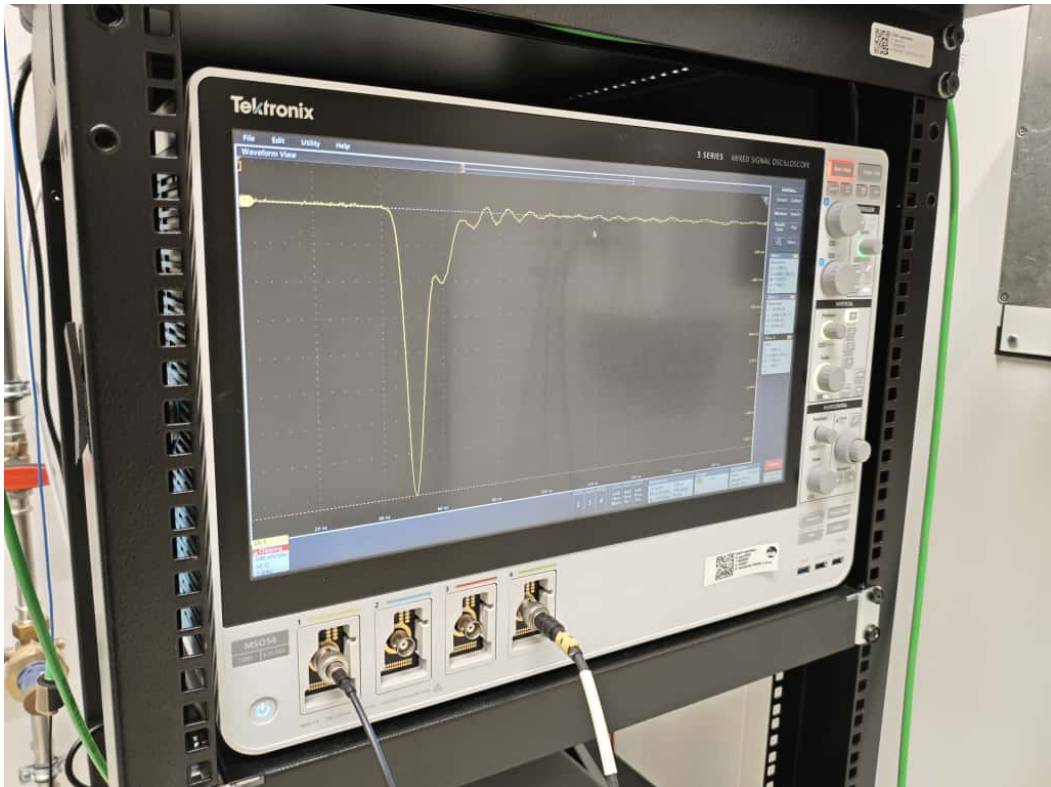


Figure 3.7: Representative PMT pulse on the MSO54 together with the acquisition settings visible in a window at bottom (6.25 GS/s, 200 ns, 20 ns/div). The displayed pulse is generated from one of the ANTARES PMTs.

3.4 Acquisition settings and procedure

Before starting to record waveforms from each ANTARES PMT, the HV is kept on for about 20 minutes. This is done to let the dark current settle, which is initially higher due to thermionic emission or residual gas ionisation. This then gradually decreases when cathode and dynodes equilibrate under the applied field, and absorbed gases on the surfaces are reabsorbed or neutralised.

The measurement proceeds over an HV ladder from a lower starting HV (between 1100V and 1200V) up to a higher operating HV (between 1500V to 1600V), in uniform steps of 100V. At each HV point I wait for stabilization, then record a fixed number (10,000 waveforms) of triggered waveforms in sequence mode. Periodically, short dark runs (laser off) are also done to monitor baseline noise and dark-count activity. Trigger level and polarity are set to capture the full pulse with adequate pre- and post-samples inside the 200 ns window.

Inside the dark box, the 10" PMT sits in the custom cradle; the fiber is aimed at the center of the photocathode and kept at a fixed stand-off for the entire period of thesis (as already shown in Figure 3.2b).

Logging of several controls during data taking is done:

- **Baseline and noise:** short runs with HV on/laser off to track noise floor and identify potential light leaks.
- **Delay in pulse generator:** The desired delay of 140ns is fed to the pulse generator to ensure the position of waveform remains at a desired uniform place (50ns in the 200ns window).
- **Saturation watch:** quick amplitude check at every HV setting to ensure pulses remain within the linear vertical range.
- **Cable/impedance check:** stable pulse shape and no ringing indicate good matching along the pick-off-scope chain.
- **Laser stability:** occupancy monitored over time; any drift triggers a short alignment check.

The entire procedure, which includes setting the instruments to the correct configurations, starting the measurements, recording the waveforms, saving the data, and performing the necessary calculations and analysis, is automated by the Python scripts developed during the period of my thesis. These scripts allows to control of all instruments remotely via LAN (SCPI over TCP/IP via PyVISA), except for the high voltage (HV) equipment, which must be adjusted manually each time.

3.4.1 ANTARES optical-module extraction (context)

The 10" PMTs used in this work were previously extracted from ANTARES optical modules (OMs) by a group of colleagues at ECAP before the start of the measurements. An ANTARES OM is a pressure-resistant glass sphere that houses the PMT with a μ -metal shield, the divider base, and ancillary cabling, all fixed in an optically clear potting gel. Extraction, therefore, has three practical constraints: (i) opening the sphere safely without cracking or implosion-like failures, (ii) separating the PMT and base from the gel without breaking the neck, and (iii) preserving the photocathode surface and HV contacts from contamination. In practice, the sphere is secured in a padded cradle, the equatorial seal is carefully released, and the two hemispheres are lifted apart under full PPE. The gel around the PMT front is cut back in small steps; residual gel on the envelope is later removed with approved solvents and lint-free wipes. These PMTs are then kept for several weeks in a dark place with dark black plastic covers. Only then are these PMTs tested in the dark room lab [21].



(a) ANTARES PMT before extraction



(b) ANTARES PMTs after extraction

Figure 3.8: (a) ANTARES PMTs inside their original optical modules (OMs) prior to extraction, each containing a 10" PMT enclosed within a glass sphere and (b) the same PMTs after extraction, prepared for gain testing. Adapted from [21]

4 Data Analysis Methods

4.1 Overview of the workflow

The whole workflow is carried out with the help of python scripts and is pretty straightforward. The workflow is as follows: (i) acquire waveforms with stable timing and low metadata; (ii) apply reproducible preprocessing—voltage calibration, baseline estimation, and fixed integration windows—form charge histograms; (iii) fit a parametric photomultiplier response model; (iv) extract the gain for each HV; and (v) fit the gain-HV dependence to derive the nominal bias for the target gain. In practice, the procedure is divided into small, focused scripts: one operates the instruments and writes data; one performs quick-look quality checks; one executes the physics analysis (histograms, peak/valley logic, model fits); and a thin summary stage aggregates per-PMT results and renders the gain–HV calibration. Each piece is small on purpose, so that if anything misbehaves, it is easy to pinpoint.

4.2 Data structure and metadata

Waveforms and results are stored in a single HDF5 file per PMT. From the analysis point of view, each HV setting corresponds to one dataset containing a sequence of frames of uniformly sampled waveforms. The data saving is hierarchical: a top-level metadata block stores the PMT serial number (SR) and tags; each HV group stores the waveform array(s), basic acquisition parameters (samplerate, record length, vertical scale/offset, timestamp, number of frames), and a dedicated area to save the analysis products (integration

windows, valley coordinate, fitted parameters with uncertainties, and compact quality flags). The structure is intentionally minimal but explicit, so that later stages can be re-run easily.

4.3 Preprocessing and charge definition

4.3.1 Voltage calibration and baseline.

Raw digital samples are converted to volts using the recorded and saved scale (YMUL) and offset (YOFF). A pedestal region (baseline window) precedes the pulse; its mean \bar{V}_{ped} is used for baseline subtraction.

4.3.2 Integration windows and charge proxy.

A fixed signal window (200ns) confines the full anode pulse. For an event trace V_i with sample period Δt , pedestal window indices $i \in [p_{\min}, p_{\max}]$ and signal window indices $i \in [s_{\min}, s_{\max}]$, the per-event charge proxy (volt-seconds) is

$$Q = - \sum_{i=s_{\min}}^{s_{\max}} (V_i - \bar{V}_{\text{ped}}) \Delta t, \quad \bar{V}_{\text{ped}} = \frac{1}{N_{\text{ped}}} \sum_{i=p_{\min}}^{p_{\max}} V_i, \quad (4.1)$$

with the minus sign reflecting negative pulses at the anode. For a given HV series the same $(p_{\min}, p_{\max}, s_{\min}, s_{\max})$ are kept unless diagnostics require a retune. To check the routine diagnostics, the average waveform is examined with both windows together to ensure the baseline is even and the pulse is complete.

4.3.3 Robustness to window choice.

Sensitivity to window edges is assessed by scanning (s_{\min}, s_{\max}) on a coarse grid for a representative high voltage (HV) point. A trustworthy setup shows a stable plateau in the reconstructed gain G as long as the pulse is included and ringing is prevented. The main results rely on a single, fixed window set for each HV series.

4.4 Charge spectrum and valley logic

In each HV point, the $\{Q\}$ distribution is accumulated into a charge histogram. Binning is chosen to resolve the pedestal peak and the SPE peak without oversampling the tails. The code first identifies the pedestal maximum on the left, searching then at a safe offset on the right for the first local minimum. This minimum is the valley. Intuitively, the valley marks the transition between the pedestal-dominated region (electronics noise, dark counts) and the onset of photoelectron populations. Its position is recorded as Q_{val} and the peak-to-valley ratio,

$$P/V = \frac{H_{\text{ped,peak}}}{H(Q_{\text{val}})},$$

for quick quality indicators for each HV point.

How the code finds a reliable valley (and when it can fail): To avoid single-bin noise, the search in the script uses a light smoothing of the histogram counts (a short moving average). Then it looks for the first zero-crossing of the discrete derivative to the right of the pedestal peak, restricted to a reasonable window. The offset from the pedestal peak and the allowable search range are fixed for a whole HV series, which keeps the valley definition consistent. In complicated cases, such as under-amplified shoulders or very high occupancy, the minimum can flatten. In this scenario, the algorithm falls back to a median-filtered profile and applies a weak monotonicity constraint to ensure that Q_{val} does not drift left of an SPE-seeded threshold. The position uncertainty is set by rebinning (coarse/fine) and by bootstrap resampling of frames; I store the resulting spread $\sigma(Q_{\text{val}})$ together with P/V. In practice, the automatic choice is stable for most data. However, if needed, the index can be nudged manually by a separate function created within the same script, but only with the same rule applied coherently to the complete HV series.

4.5 Parametric response model and two-stage estimation

4.5.1 Model

The measured charge spectrum is modelled as a pedestal plus a sum over n -photoelectron contributions. After the integration of multiplication statistics with electronics noise, the n -pe component is well approximated by a Gaussian with mean and variance that scale with n . The full model reads

$$f(Q) = A_0 \mathcal{N}(Q; \mu_{\text{ped}}, \sigma_{\text{ped}}^2) + \sum_{n=1}^N A_n \mathcal{N}(Q; \mu_{\text{ped}} + n q_{\text{spe}}, \sigma_{\text{ped}}^2 + n \sigma_{\text{spe}}^2), \quad (4.2)$$

where q_{spe} is the mean SPE charge and σ_{spe} characterizes its spread; $(\mu_{\text{ped}}, \sigma_{\text{ped}})$ describe the baseline. The weights A_n follow a Poisson law with mean occupancy λ (cut off to the finite fitted range). In some cases, a shallow under-amplified shoulder near the valley is effectively absorbed by a slightly larger variance in the $n=1$ term.

4.5.2 Two-stage estimation and rationale.

A single, global fit of Eq. (4.2) can converge slowly or latch onto local minima when initial values are not perfect. To stabilise the problem, a two-stage scheme is used:

1. **Pre-fit (local, robust):** estimate $\mu_{\text{ped}}, \sigma_{\text{ped}}$ from the pedestal region and $(q_{\text{spe}}, \sigma_{\text{spe}})$ from a narrow SPE slice around the first peak using simple Gaussians. This produces well-behaved seeds that are largely insensitive to tails and small multi-pe shouldered.
2. **Global fit (full model):** initialize with the pre-fit values and fit Eq. (4.2) over the full histogram range with Poisson weights turned on, subject to physical bounds. The global fit returns parameter estimates and the covariance matrix used downstream.

This separation keeps the pre-fit numerically reasonable and robust, and lets the second pass focus on extracting physically meaningful parameters with controlled uncertainties.

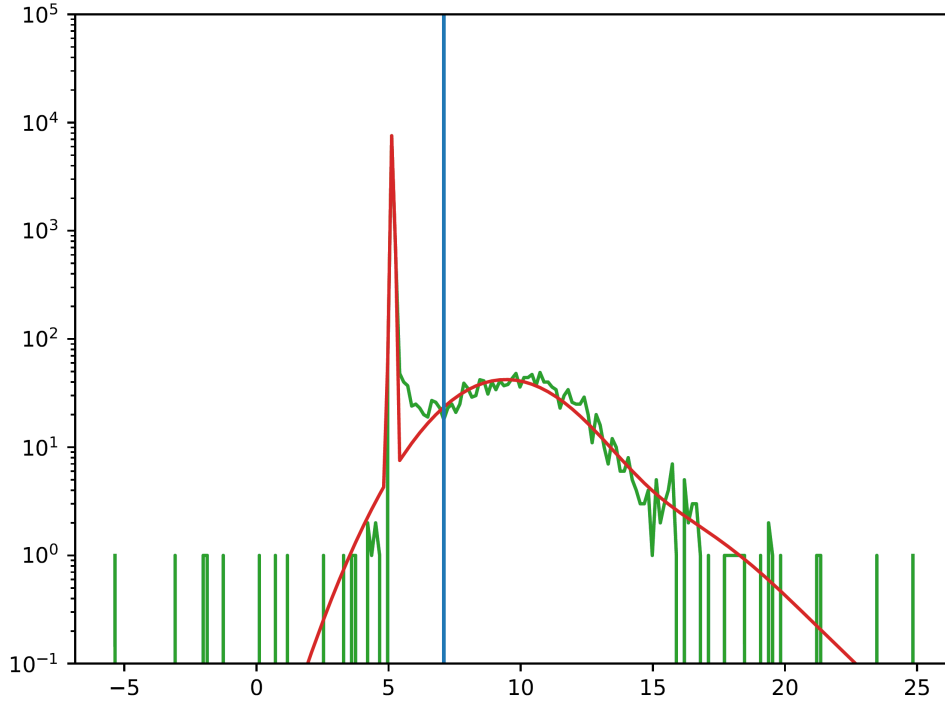


Figure 4.1: Charge spectrum at a representative HV point. Green — base-line-subtracted histogram of integrated charge Q (logarithmic y -axis). Red — parametric response fit (pedestal + SPE + higher n -pe components). Blue vertical line — automatically determined valley Q_{val} used as a guard rail for the fit and for the P/V diagnostic.

4.6 Gain extraction and propagated uncertainties

From the fitted q_{spe} the gain follows directly. With a resistive load $R = 50 \Omega$ and the elementary charge e ,

$$G = \frac{q_{\text{spe}}}{R e}, \quad \text{with} \quad q_{\text{spe}} \equiv \sum_{i \in \text{sig}} (V_i - \bar{V}_{\text{ped}}) \Delta t. \quad (4.3)$$

Uncertainties are propagated from the covariance matrix of the global fit. In the simplest (dominant) term,

$$\sigma_G = \frac{\sigma(q_{\text{spe}})}{R e}, \quad (4.4)$$

and correlations between fitted parameters are retained where relevant. For each HV point the analysis records (G, σ_G) together with diagnostic figures of merit such as P/V and λ .

4.7 Gain-voltage calibration and nominal operating voltage

The gain as a function of HV is modeled by a power law,

$$G(\text{HV}) = G_0 \left(\frac{\text{HV}}{\text{HV}_0} \right)^\kappa \iff \log_{10} G = a + \kappa \log_{10} \text{HV}, \quad (4.5)$$

which is fitted as a straight line in $(\log_{10} \text{HV}, \log_{10} G)$ with weights derived from σ_G . From the best-fit slope κ and intercept a we obtain the bias that yields the target gain,

$$\text{HV}_{\text{nom}}(G=5 \times 10^7) = 10^{\left(\log_{10}(5 \times 10^7) - a \right) / \kappa}, \quad (4.6)$$

and propagate the uncertainty on HV_{nom} using the full fit covariance (including the a - κ correlation). The final calibration plot shows the measured points with uncertainties, the fitted line in log-log space, the horizontal line at $G = 5 \times 10^7$, and the corresponding HV_{nom} .

Gain-voltage calibration for PMT ST5498 is shown in 2.7. The points are per-HV gains with 1σ uncertainties in $\log_{10} G$. The line is the weighted linear fit in $\log_{10} G$ vs $\log_{10} \text{HV}$. The horizontal dashed line marks the target $G = 5 \times 10^7$; the vertical dashed line indicates the derived HV_{nom} . The inset reports the best-fit slope κ , intercept a , and $\text{HV}_{\text{nom}} \pm \sigma$.

4.8 Additional python scripts

Everything mentioned in this section has corresponding Python scripts. Additionally, I have created separate Python scripts for various purposes. One script is specifically designed to delete HV groups from a specified file, another allows users to view stored values within subgroups of HV groups, and a third enables users to display individual waveforms from recorded data. All the scripts I have developed and utilised for my thesis have been properly uploaded and stored in a Git repository, along with an instructional document to guide users in their usage. This Git repository can be accessed from the appendix B.

5 Results

5.1 Overview of the Measurement Procedure

For analysis, comparison and statistics, 40 ANTARES PMTs (serial number STXXXX) and 1 reference PMT (TM0007), for a total of 41 PMTs are analyzed. Each PMT was recorded at a certain high-voltage (HV) setpoints under fixed illumination. Most PMTs have four HV setpoints; and a few have five to stabilise the log–log gain calibration.

Coverage: Figure 5.1 summarises the number of HV setpoints per PMT: 31 devices with four usable HV groups and 10 with five (the five-point count includes the reference PMT). Only HV groups passing the quality selection are counted.

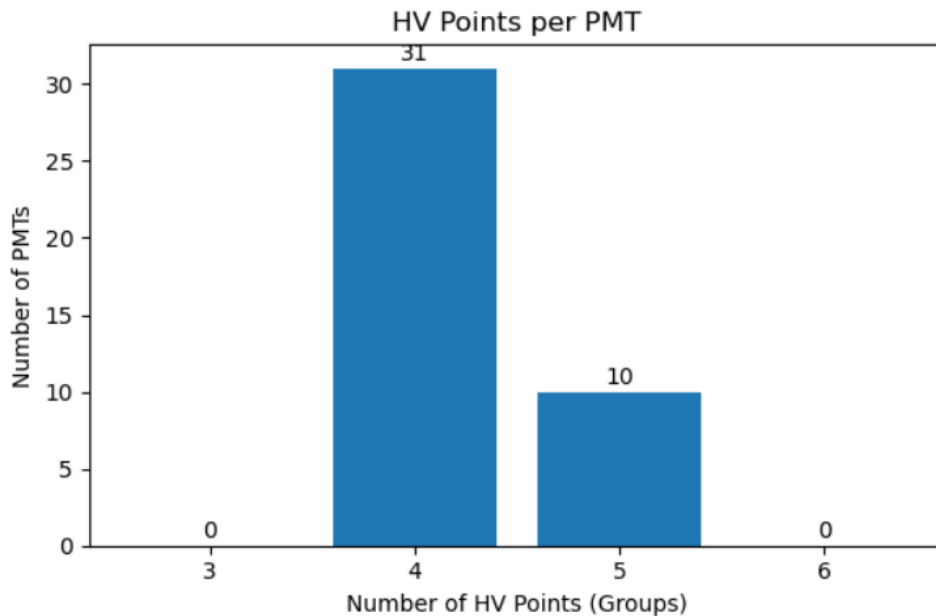


Figure 5.1: Histogram of HV scan points per PMT.

SPE occupancy: Across the analysis phase, the SPE occupancy λ remained within the intended SPE regime at all HV points (median and interquartile spread per HV are shown in Fig. 5.2). Under fixed illumination, λ is expected to be HV-independent; the flat median trend serves as a global quality check for fit stability.

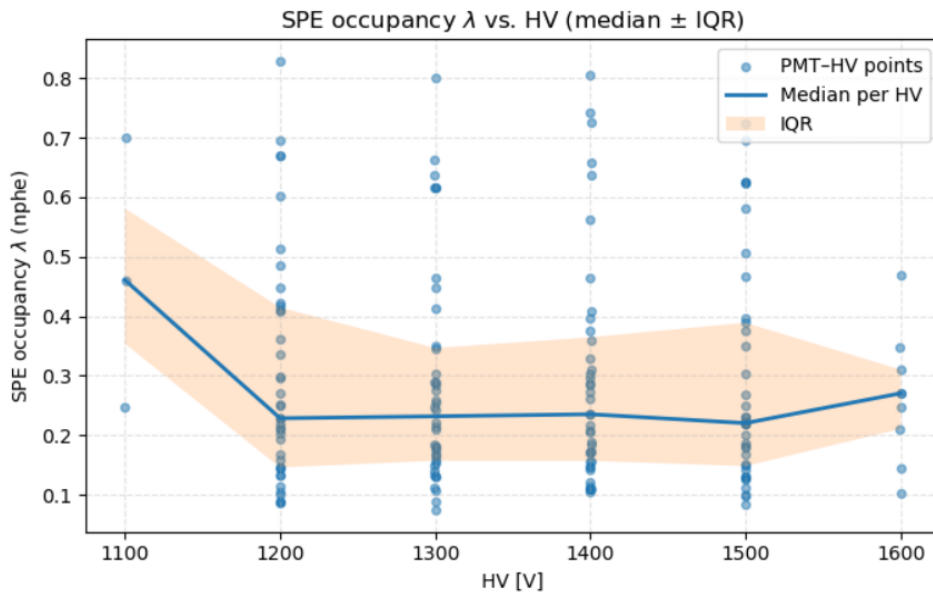


Figure 5.2: SPE occupancy λ vs. HV across all PMTs. Dots show per-PMT, per-HV λ values; the solid line is the median at each HV, and the shaded band indicates the interquartile range (IQR). The near-flat median is consistent with stable illumination and operation in the SPE regime.

To keep the results section focused on quantitative outcomes (gain–HV fits and HV_{nom}), I summarise here only the HV coverage per PMT. Table 5.1 records the number and values of HV setpoints used for each PMT; the complete per-HV metadata (including G , σ_G , and λ) is provided in Appendix A.1.

Table 5.1: PMT inventory: The HV count including the reference PMT. Full per-HV metadata is provided in Appendix A.1.

Serial	Type/Base	#HV	HV setpoints [V]
ST5228	ANTARES / R7081-20	5	1200, 1300, 1400, 1500, 1600
ST5289	ANTARES / R7081-20	4	1200, 1300, 1400, 1500
ST5311	ANTARES / R7081-20	4	1300, 1400, 1500, 1600
ST5326	ANTARES / R7081-20	4	1200, 1300, 1400, 1500
ST5332	ANTARES / R7081-20	4	1200, 1300, 1400, 1500
⋮	⋮	⋮	⋮
TM0007	Reference / R7081-20	5	1200, 1300, 1400, 1500, 1600

5.2 Gain measurements

In this section, the measured gains are presented as a function of HV and summarised per PMT and for the ANTARES set as a whole.

The extraction of gain from charge spectra and the log–log calibration procedure were described in earlier chapter; only the quantitative outcomes are shown here.

5.2.1 ANTARES PMTs

To create summaries for the whole fleet, three representative ANTARES PMTs are first highlighted: a typical case (ST6198), a best case in terms of calibration stability (ST6242), and a boundary case selected by a higher HV_{nom} within acceptance (ST5326). For each, a charge spectrum at HV of 1400V is shown together with the fitted response model, followed by the gain–HV calibration from which HV_{nom} at $G = 5 \times 10^7$ is obtained.

Representative examples: A 1400V spectrum of ST6198 is shown in Fig. 5.3. A well-separated pedestal and SPE peak are visible, and the fitted curve follows the data over the full range of counts. The corresponding calibration in Fig. 5.4 exhibits an approximately linear trend in $\log_{10} G$ versus $\log_{10} \text{HV}$, and the intersection with $G = 5 \times 10^7$ yields a stable HV_{nom} with a small

uncertainty. Two further examples are provided for ST6242 (best overall calibration stability and smallest propagated uncertainty) and ST5326 (edge case with a higher HV_{nom} yet acceptable fit quality).

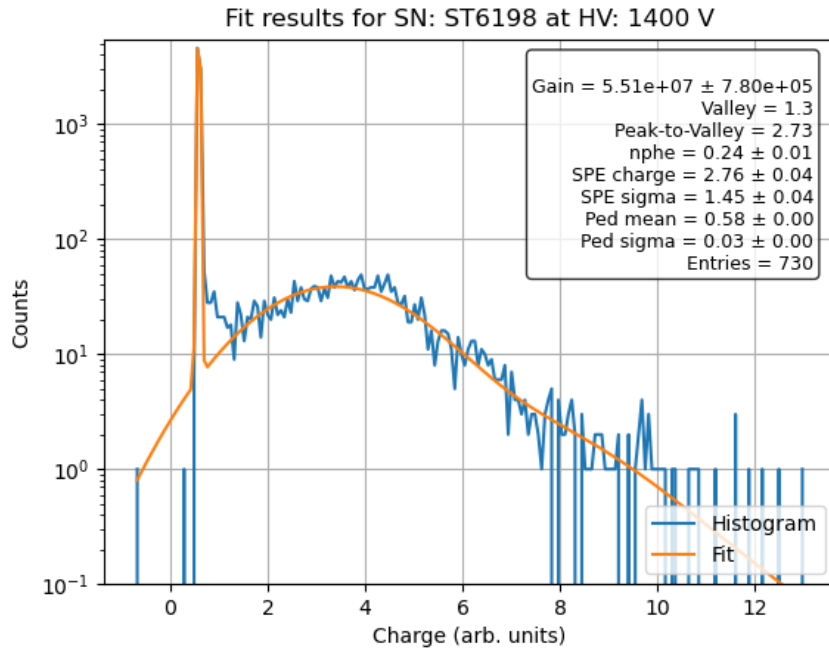


Figure 5.3: Charge spectrum at 1400V for PMT ST6198 with the fitted response overlaid. Fit diagnostics are reported in the text.

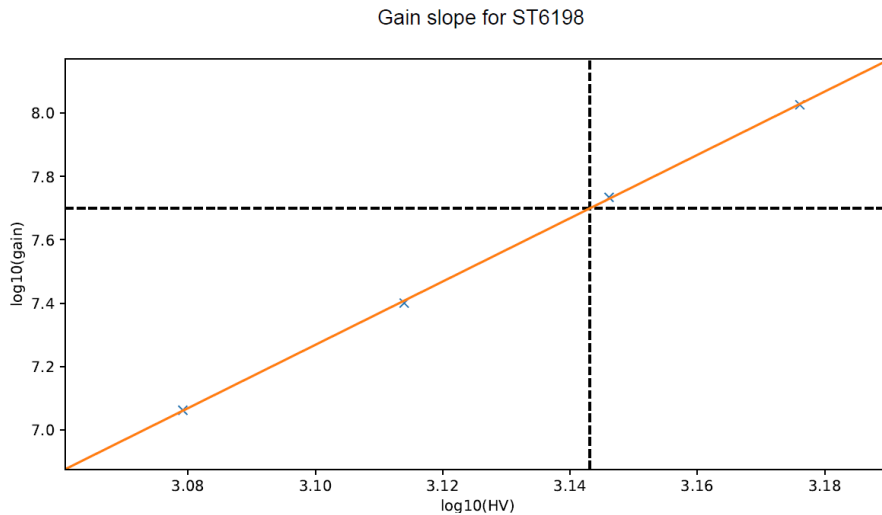


Figure 5.4: Calibration of $\log_{10} G$ versus $\log_{10} HV$ for PMT ST6198. The best-fit slope κ and the derived HV_{nom} at $G = 5 \times 10^7$ (vertical line).

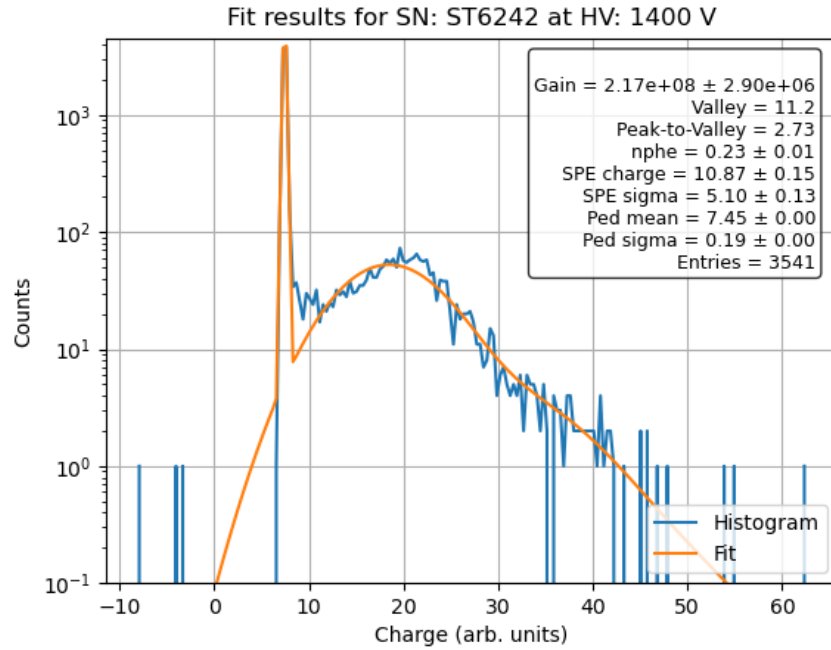


Figure 5.5: Charge spectrum at 1400V for PMT ST6242 with the fitted response overlaid.

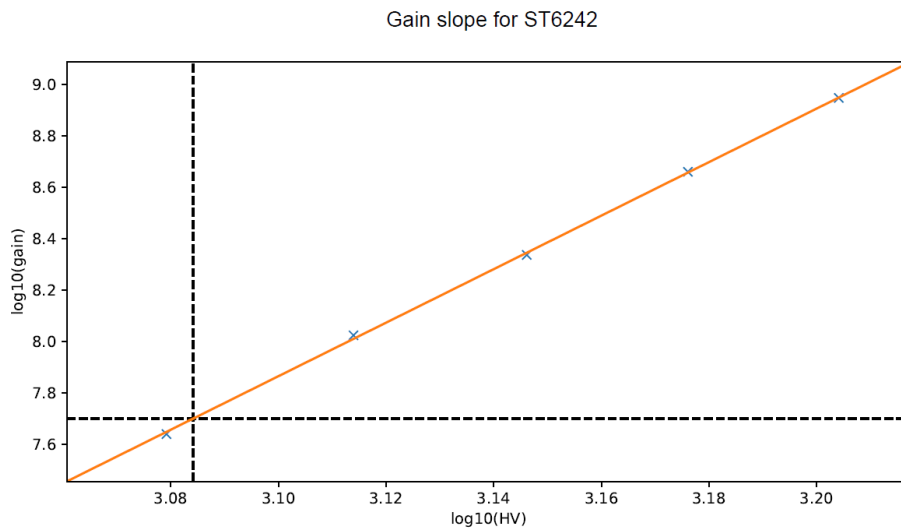


Figure 5.6: Calibration of $\log_{10} G$ versus $\log_{10} \text{HV}$ for PMT ST6242 with the derived HV_{nom} at $G = 5 \times 10^7$ (vertical line).

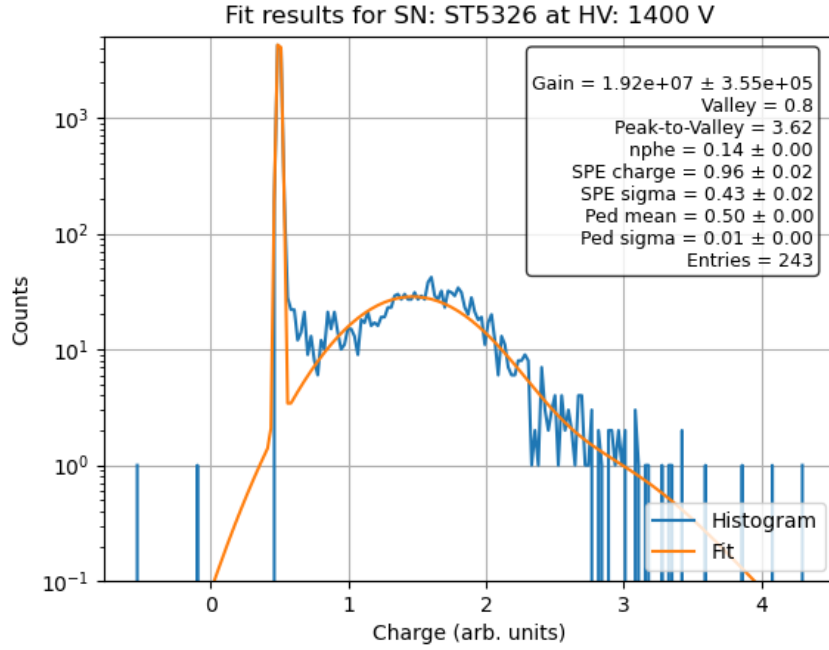


Figure 5.7: Charge spectrum at 1400V for PMT ST5326 (edge case) with the fitted response overlaid.

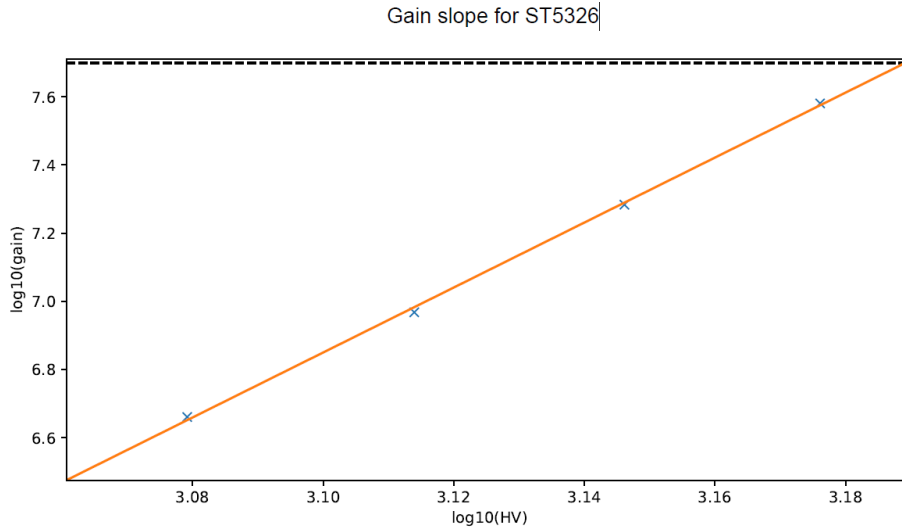


Figure 5.8: Calibration of $\log_{10} G$ versus $\log_{10} HV$ for PMT ST5326 with the derived HV_{nom} at $G = 5 \times 10^7$ (vertical line).

The fitted slopes κ cluster tightly across ANTARES PMTs (Fig. 5.9). A median of 10.1 and an interquartile range [9.9, 10.3] are observed, with mean 10.1 and standard deviation 0.3; the full range spans 9.47 to 10.64. This

narrow spread indicates a broadly uniform gain–HV scaling, with only mild variation across PMTs in how rapidly the gain rises with HV. No separate subpopulations are apparent in the histogram.

The distribution of HV_{nom} at $G = 5 \times 10^7$ (Fig. 5.10) shows a compact central bulk around the median 1388.5 V, with interquartile range [1335.5, 1470.8] V. The mean is 1397.6 V with a standard deviation of 82.2 V; the observed span extends from 1213 V to 1546 V.

A joint view of HV_{nom} versus κ was plotted (Fig. 5.11) and it reveals only a weak negative trend. PMTs with slightly larger κ tend to require marginally lower HV_{nom} , as expected from the calibration law $\log_{10} G = a + \kappa \log_{10} HV$. The scatter dominates over any simple linear dependence, indicating that slope differences explain only a small fraction of the variance in HV_{nom} . The annotated points (ST6198, ST6242, ST5326) illustrate a typical, best-stability, and higher- HV_{nom} case within the accepted quality selection.

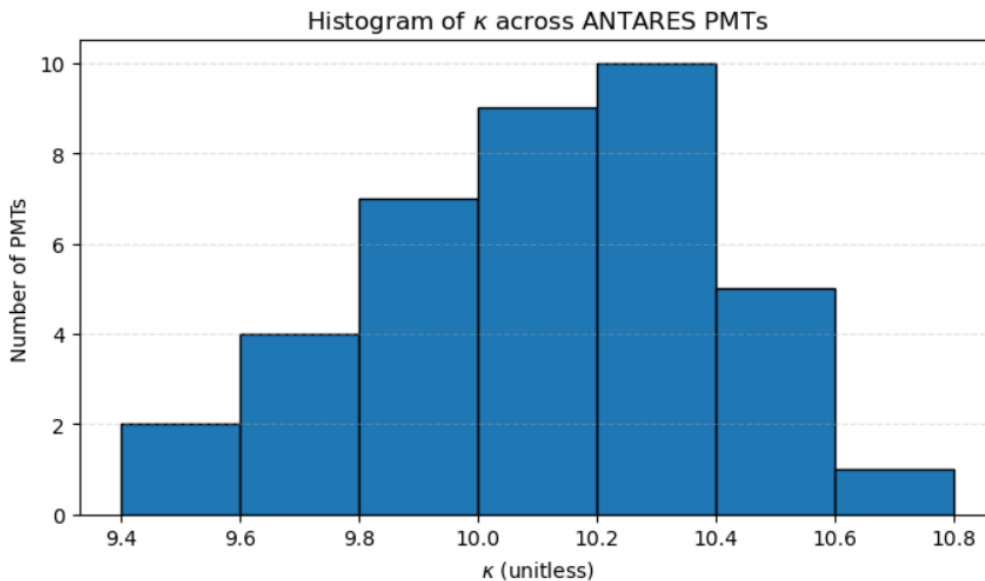


Figure 5.9: Distribution of fitted slopes κ for all ANTARES PMTs. The central tendency and spread quantify the uniformity of the gain–HV scaling.

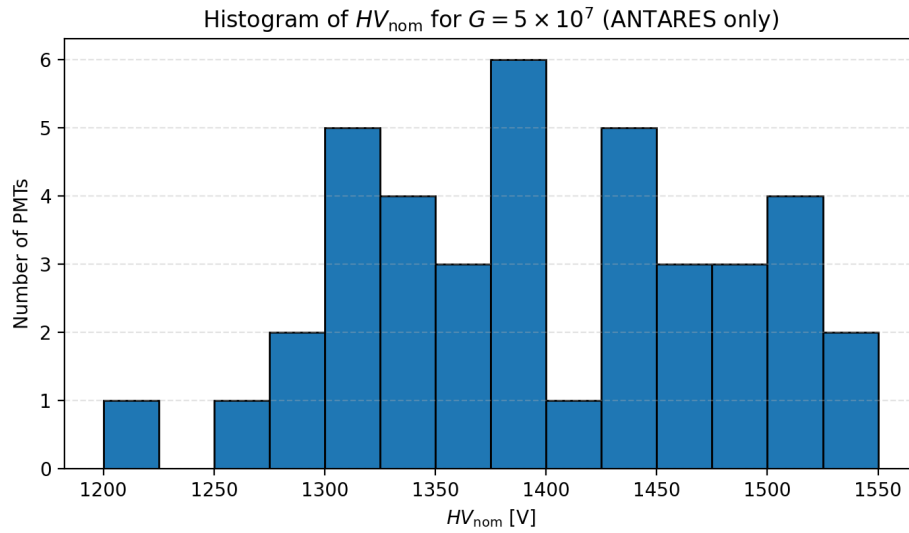


Figure 5.10: Distribution of HV_{nom} at $G = 5 \times 10^7$ for ANTARES PMTs. Entries correspond to the nominal voltages derived from each PMT's gain–HV calibration.

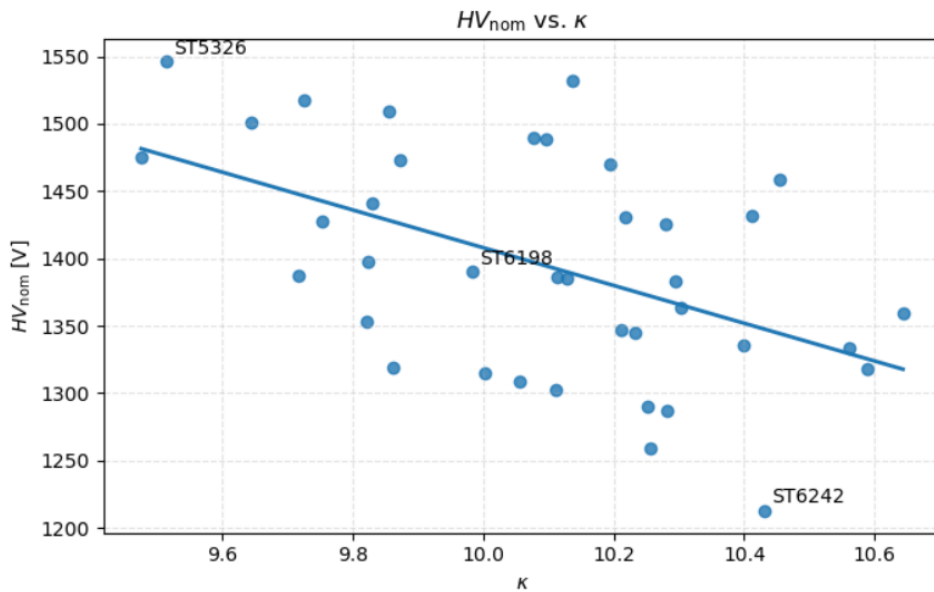


Figure 5.11: HV_{nom} versus κ for ANTARES PMTs. Each point corresponds to one PMT; a weak or null trend is expected once uncertainties are accounted for.

5.2.2 Reference PMT and group comparison

For proper comparison, a compact view of the reference PMT TM0007 is included using the same layout, followed by a direct comparison between ANTARES and reference groups.

Reference PMT (TM0007).

The 1400V HV spectrum and the gain–HV calibration are shown in Figs. 5.12 and 5.13. The extracted κ and HV_{nom} serve as a practical benchmark for the ANTARES distributions and conclusions.

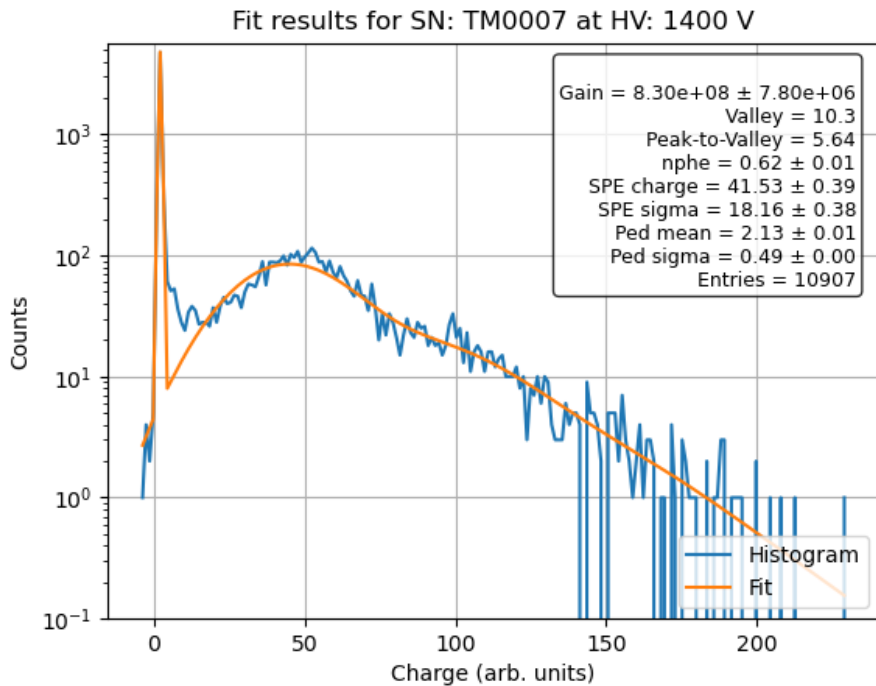


Figure 5.12: Charge spectrum at 1400V for the reference PMT TM0007 with the fitted response overlaid.

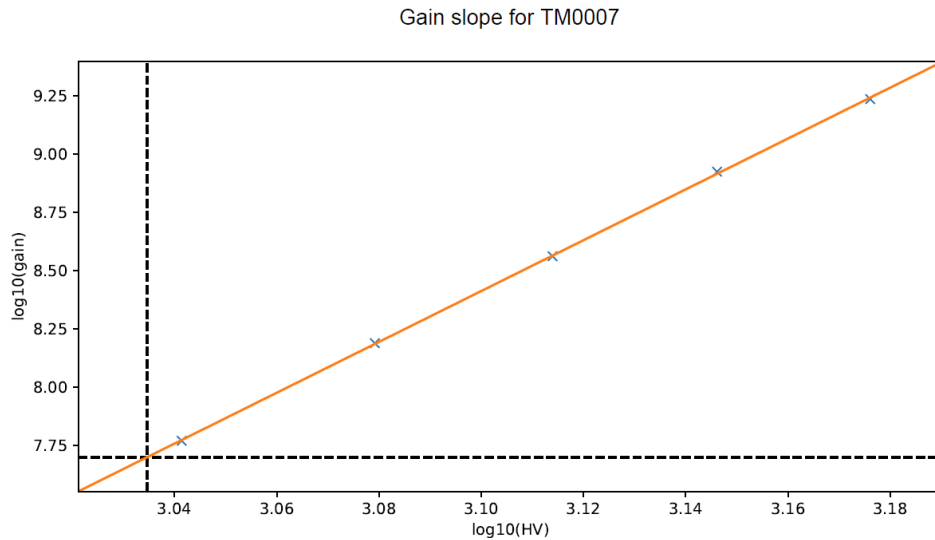


Figure 5.13: Calibration of $\log_{10} G$ versus $\log_{10} \text{HV}$ for the reference PMT TM0007 with the derived HV_{nom} at $G = 5 \times 10^7$ (vertical line).

ANTARES vs. reference (distributions)

ANTARES results are summarised as histograms as shown in Figure 5.14 and Figure 5.15 with the sample median shown as an orange line and the interquartile range (IQR) highlighted as a blue band, while the reference PMT (TM0007) is indicated by a green marker. The IQR is the interval between the 25th and 75th percentiles; it captures the middle half of the ANTARES population and is less sensitive to outliers than a full standard deviation. Including the IQR makes it clear where the bulk of ANTARES PMTs lie and allows the position of the reference to be read at a glance: a marker inside the band is “typical”, whereas a marker outside the band falls in a tail. In the present data, TM0007 lies below the ANTARES IQR for HV_{nom} and above the ANTARES IQR for κ , consistent with the visual impression from the two plots.

The results from Figure 5.14 and Figure 5.15 are mentioned in Table 5.2.

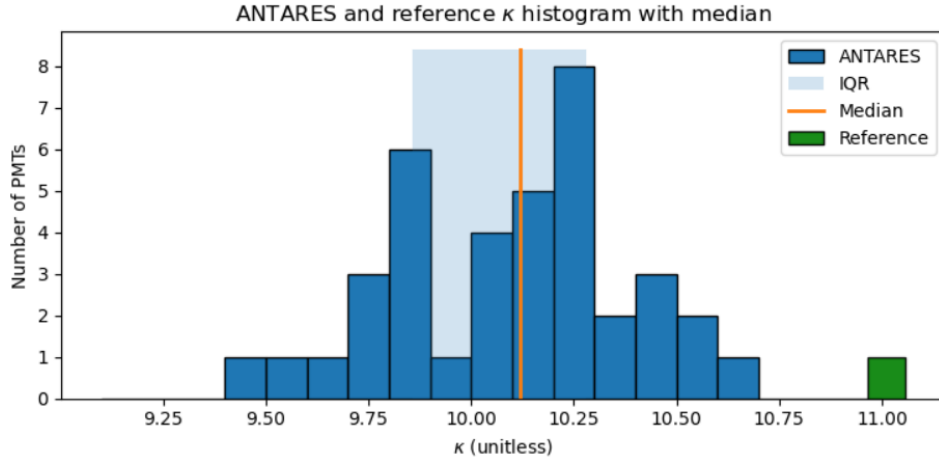


Figure 5.14: Fitted slope κ across ANTARES PMTs (histogram) with the sample median (orange) and interquartile range (IQR, blue band). The reference PMT TM0007 is marked in green at its κ value.

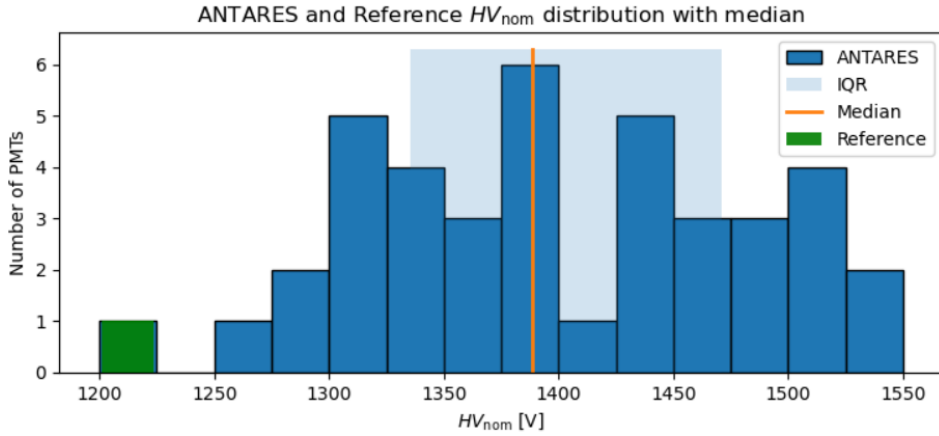


Figure 5.15: Distribution of HV_{nom} at $G = 5 \times 10^7$ for ANTARES PMTs (histogram) with the sample median (orange) and IQR (blue band). The reference PMT TM0007 is marked in green at its HV_{nom} .

Table 5.2: Reference (TM0007) vs. ANTARES median at $G = 5 \times 10^7$.

Metric	Reference	ANTARES median
κ	11	10.1
HV_{nom} [V]	1083	1388.5

5.3 Verdict on nominal HV of ANTARES PMTs

Nominal operating voltages HV_{nom} at $G = 5 \times 10^7$ are summarised for all ANTARES PMTs. The observed HV_{nom} for reference PMT (TM0007) is 1083V. In contrast, a compact central bulk is observed around the median 1388.5 V, with interquartile range (IQR) [1335.5, 1470.8] V. The mean and standard deviation are 1397.6 V and 82.2 V, respectively, and the observed span extends from 1213 V to 1546 V. These values indicate that most ANTARES PMTs operate near 1400 V at the target gain, with a modest tail toward higher voltages.

Figure 5.16 shows the empirical cumulative distribution (CDF) of HV_{nom} for the fleet. The dashed vertical line marks the median, and the shaded band indicates the IQR, i.e. the middle 50 % of PMTs. The IQR is shown to provide a strong idea of spread that is less sensitive to outliers than the standard deviation. A high-percentile marker is included to illustrate supply headroom; in the present data it lies near 1500 V, indicating that about nine out of ten PMTs require ≤ 1500 V at $G = 5 \times 10^7$.

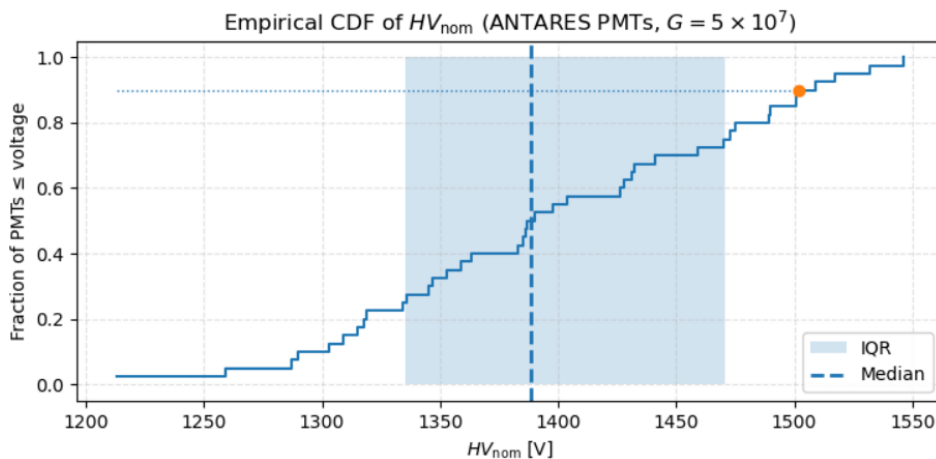


Figure 5.16: Empirical CDF of HV_{nom} for ANTARES PMTs at $G = 5 \times 10^7$. The dashed line marks the median; the shaded band shows the interquartile range (IQR, 25–75 %). The orange point illustrates a high-percentile operating voltage (near the 90th percentile).

For deployment, a per-PMT summary is provided in Table 5.3, listing HV_{nom} with its propagated uncertainty.

Table 5.3: Final HV_{nom} per selected ANTARES PMTs as well as reference PMT, with propagated 1σ uncertainty. Rows include ST6198 (typical), ST6242 (best), ST5326 (edge), plus informative extremes and a near-median entry. The full fleet appears in Appendix A.

Serial	HV_{nom} [V]	$\sigma(HV_{\text{nom}})$ [V]
ST6242	1214	4
ST6198	1390	2
ST5326	1546	4
TM0007	1083	1
ST6003	1334	4
ST6345	1335	2
ST6277	1470	2
ST5628	1474	3

Operational note: On the basis of the CDF and IQR, the vast majority of ANTARES PMTs fall within ~ 1250 – 1550 V at the target gain, compatible with typical SWGO HV supplies.

6 Conclusions

6.1 Summary of Aims and Approach

The work presented in this thesis was done to determine if ANTARES PMTs can be reused in the SWGO with minimal performance compromises and clear operational margins. Importantly, the nominal high voltages HV_{nom} have been derived for each ANTARES PMT in comparison with a new reference PMT at a target gain of $G = 5 \times 10^7$, the gain–HV relation has been quantified through a power-law slope κ , and fleet-level statistics have been determined for both to inform selection ranges and integration pathways for SWGO deployments. A reproducible analysis has been taken care of: low-light conditions were stable, SPE charge spectra were formed, and parametric response fits across 4–5 HV points per PMT were done. After fitting, the κ parameters were propagated to obtain HV_{nom} and its uncertainty at the target gain. I performed quality checks to ensure that the SPE rules were followed and to assess how well the dynamic range is represented in log–log fits.

6.2 Result discussions

6.2.1 Fleet-level operating voltages and slopes

A coherent picture of operating points has emerged. At $G = 5 \times 10^7$, the distribution of HV_{nom} is centred at a median of ~ 1388.5 V, with an interquartile range of [1335.5, 1470.8] V. The mean is ~ 1397.6 V with a standard deviation of about 82 V, and the observed span across the measured samples is 1213–1546 V. In practical terms, the majority of PMTs can be operated below

1500 V at the target gain, leaving comfortable headroom for standard SWGO front-end bases and high-voltage channels.

The gain–HV slope κ was found to populate a compact band consistent with expectations for large-area PMTs (like ANTARES PMTs) in SPE conditions. No evidence for distinct sub-populations was observed. A very weak anti-correlation between HV_{nom} and κ is present, which is fully consistent with the power-law form $\log_{10} G = a + \kappa \log_{10} HV$: steeper κ typically implies a slightly lower HV_{nom} at fixed target gain.

6.2.2 Reference cross-check

A reference PMT (TM0007) was analysed with the same procedure and works as a useful reference point. Its slope is $\kappa \approx 11$, and its HV_{nom} is ≈ 1083 V at $G = 5 \times 10^7$. Within the fleet statistics, TM0007 sits below the interquartile band in HV_{nom} and on the higher side of the κ distribution, which matches expectations for a particularly new and responsive PMT.

6.2.3 Data quality, uncertainties, and robustness

Charge histograms at each HV were accumulated in a method of low occupancy to isolate the SPE peak from the pedestal with stable separation via valley. The fits to the SPE response model were bound by multiple HV points per PMT, and the covariance between a and κ was retained when propagating uncertainties to HV_{nom} . Stability checks on the illumination and on the internal valley parameters of the charge spectra indicate that the extraction of κ and HV_{nom} is robust against modest fluctuations. Outlier-resilient summaries (median and IQR) were preferred for fleet-level statements to reduce the influence of tails.

6.3 Implications for SWGO Reuse

The central outcome is encouraging: most ANTARES PMTs reach $G = 5 \times 10^7$ at voltages that are fully compatible with SWGO electronics and power

constraints. From an integration standpoint, an ensemble operated around the $\sim 1.35\text{--}1.50$ kV band is straightforward to service, simplifies high-voltage distribution, and reduces stress on bases. In addition, the narrowness of the κ distribution suggests that channel-to-channel gain tuning will be efficient and that uniform calibration procedures can be applied across a large fraction of the fleet.

The conclusive outcome is promising for SWGO! Most ANTARES PMTs reach $G = 5 \times 10^7$ at the values of voltages that are fully compatible with SWGO electronics and power constraints. For integration, running the array in the 1350–1500 V range makes servicing straightforward, simplifies HV distribution, and reduces stress on the bases. Also, the tight κ -distribution means per-channel gain tweaks work well, and a single calibration method can cover most of the fleet.

A direct transfer step has already been initiated. Four characterised PMTs have been selected from ECAP and shipped to the SWGO USA group for evaluation under SWGO-like conditions with the relevant front-end electronics and timing environment. If everything goes well, these PMTs may serve among the first installed channels during the initial SWGO build stage. This step is expected to tighten the loop between laboratory characterisation and system-level performance metrics (dynamic range, noise, and timing), thereby accelerating the definition of acceptance bands for broader reuse.

6.4 Limitations of this thesis

Several limitations should be noted. First, while the current sample is representative of the available stock, it does not yet constitute a full population study; tails and corner cases may therefore be under-sampled. Second, absolute light calibration was held stable by design, but a formal transfer to the illumination scales and monitoring practices of the SWGO integration system can further help this study. Third, environmental dependencies—such as temperature, ambient magnetic field, and base-to-base differences—were not stress-tested here and should be included in follow-up studies. Finally, only gain and SPE-shape related quantities were used for the primary selection; complementary parameters like dark rate, afterpulsing probability,

and transit-time spread (TTS) require dedicated runs which will give further statistics to the results.

6.5 Closing Statement

In summary, it has been demonstrated that a substantial fraction of ANTARES PMTs can be operated at $G = 5 \times 10^7$ with moderate high voltages and with a compact spread of gain–HV slopes. The quantitative distributions obtained here support the feasibility of reuse within SWGO, both from an operational and a calibration standpoint. With four characterised PMTs already forwarded for system-level testing, the path from laboratory characterisation to field deployment is now open. These results therefore provide a practical and cost-effective route to accelerating early SWGO readiness while aligning with sustainability goals.

Bibliography

- [1] A. Aab et al. “A Search for Point Sources of EeV Photons”. In: *The Astrophysical Journal* 789.2 (2014), p. 160. DOI: [10.1088/0004-637X/789/2/160](https://doi.org/10.1088/0004-637X/789/2/160).
- [2] A. U. Abeysekara et al. “Observation of the Crab Nebula with the HAWC Gamma-Ray Observatory”. In: *The Astrophysical Journal* 843 (2017), p. 39.
- [3] P. Abreu, R. Alfaro, A. Alfonso, et al. “Science Prospects for the Southern Wide-field Gamma-ray Observatory: SWGO”. In: *arXiv preprint* (2025). arXiv: [2506.01786](https://arxiv.org/abs/2506.01786) [astro-ph.HE].
- [4] Hanieh Alaeian. *An Introduction to Cherenkov Radiation*. Stanford University course article, accessed October 2025. 2014.
- [5] J. Blümer, R. Engel, and J. R. Hörandel. “Cosmic Rays from the Knee to the Highest Energies”. In: *Progress in Particle and Nuclear Physics* 63 (2009), pp. 293–338. DOI: [10.1016/j.pnpnp.2009.05.002](https://doi.org/10.1016/j.pnpnp.2009.05.002).
- [6] Z. Cao et al. “Ultrahigh-Energy Photons up to 1.4 PeV from 12 Gamma-Ray Galactic Sources”. In: *Nature* 594 (2021), pp. 33–36.
- [7] Juan de Dios Zornoza and Juan Zúñiga. “The ANTARES Neutrino Telescope”. In: *Highlights of Spanish Astrophysics VII, Proceedings of the X Scientific Meeting of the Spanish Astronomical Society*. Valencia, Spain: Spanish Astronomical Society (SEA), July 2012, pp. 651–658.
- [8] I. M. Frank and I. E. Tamm. “Coherent Visible Radiation of Fast Electrons Passing Through a Medium”. In: *Doklady Akademii Nauk SSSR* 14 (1937), pp. 109–114.

- [9] T. K. Gaisser and T. Stanev. “Cosmic Rays”. In: *Frontiers of Physics* 8 (2016), pp. 748–758. DOI: [10.1007/s11467-013-0319-7](https://doi.org/10.1007/s11467-013-0319-7).
- [10] Hamamatsu Photonics K.K. *Large Photocathode Area Photomultiplier Tubes*. Electron Tube Division, Japan, Technical Information Document TPMH1376E. 2017.
- [11] J. A. Aguilar et al. “ANTARES: The First Underwater Neutrino Telescope”. In: *Nuclear Instruments and Methods in Physics Research Section A* 656 (2011), pp. 11–38. DOI: [10.1016/j.nima.2011.06.103](https://doi.org/10.1016/j.nima.2011.06.103).
- [12] J. D. Jackson. *Classical Electrodynamics*. 3rd. John Wiley & Sons, 1998.
- [13] R. Joshi. “Extensive Air Showers and Cosmic Ray Detection”. In: *Current Science* 116.6 (2019), pp. 923–929.
- [14] Hamamatsu Photonics K.K. *R7081-20 Base Circuit Schematic*. Internal schematic document. 2023.
- [15] K.-H. Kampert and M. Unger. “Measurements of the Cosmic Ray Composition with Air Shower Experiments”. In: *Astroparticle Physics* 35 (2012), pp. 660–678. DOI: [10.1016/j.astropartphys.2012.02.004](https://doi.org/10.1016/j.astropartphys.2012.02.004).
- [16] Glenn F. Knoll. *Radiation Detection and Measurement*. 4th. John Wiley & Sons, 2010. ISBN: 978-0470131480.
- [17] A. Kooijman. *Tests of the Hamamatsu R7081-20 Photomultiplier for ANTARES*. Tech. rep. ANTARES Collaboration / University of Amsterdam, 2002.
- [18] Florian Leitl. “Design Studies for the Southern Wide-field Gamma-ray Observatory (SWG0)”. Master’s thesis. Erlangen, Germany: Friedrich-Alexander-Universität Erlangen-Nürnberg, 2021.
- [19] W. R. Leo. *Techniques for Nuclear and Particle Physics Experiments: A How-To Approach*. 2nd. Berlin, Heidelberg: Springer, 1994. DOI: [10.1007/978-3-642-57920-2](https://doi.org/10.1007/978-3-642-57920-2).
- [20] J. Matthews. “A Heitler Model of Extensive Air Showers”. In: *Astroparticle Physics* 22 (2005), pp. 387–397. DOI: [10.1016/j.astropartphys.2004.09.003](https://doi.org/10.1016/j.astropartphys.2004.09.003).

- [21] Alison Mitchell. *PMT Activities at ECAP*. Conference presentation: SWGO Collaboration Meeting. Sept. 11, 2024.
- [22] P. Amram et al. “The ANTARES Optical Module”. In: *Nuclear Instruments and Methods in Physics Research Section A* 484 (2002), pp. 369–383. DOI: [10.1016/S0168-9002\(02\)01530-3](https://doi.org/10.1016/S0168-9002(02)01530-3).
- [23] Diana Pawlicki, Krzysztof Stasiak, and Zbigniew Szadkowski. “Multi-Stage Adaptive Filtering of Cosmic Ray Signal Data – Application and Configuration for Ultra-High-Energy Cosmic Ray Study at Pierre Auger Observatory”. In: *Proceedings of the 75th International Astronautical Congress (IAC)*. Milan, Italy: International Astronautical Federation (IAF), Oct. 2024. DOI: [10.52202/078355-0135](https://doi.org/10.52202/078355-0135).
- [24] *Photomultiplier Tubes: Basics and Applications*. 2nd. Hamamatsu Photonics K.K. Hamamatsu City, Japan, 1994.
- [25] *Photomultiplier Tubes: Basics and Applications*. 3rd. Hamamatsu Photonics K.K. 2007.
- [26] Martin Rongen. *Hardware Crash Course for Analyzers (Bärnfels Astroparticle School 2024)*. Zenodo. Lecture slides. 2024.
- [27] S. Adrián-Martínez et al. “The First Results of the ANTARES Neutrino Telescope”. In: *Astroparticle Physics* 34 (2012), pp. 652–662.
- [28] S. Aiello et al. “The KM3NeT Neutrino Telescope”. In: *Journal of Instrumentation* 16 (2021), P07037.
- [29] Johannes Schäfer. *Gamma-ray telescope worldmap*. Version 1.0. Oct. 2025. DOI: [10.5281/zenodo.17389794](https://doi.org/10.5281/zenodo.17389794).
- [30] A. J. Smith. “Water Cherenkov Detectors in Astroparticle Physics”. In: *Annual Review of Nuclear and Particle Science* 66 (2016), pp. 145–166.

A Additional Data Tables

Table A.1: HV metadata with serial numbers (SN), type/base, HV setpoint, fitted gain (G), its uncertainty (σ_G), and SPE occupancy λ . Only HV groups passing the quality selection are listed.

SN	Type/Base	HV [V]	G	σ_G	λ
ST5228	ANTARES / R7081-20	1200	1.14×10^7	1.21×10^5	0.418
ST5228	ANTARES / R7081-20	1300	2.68×10^7	3.03×10^5	0.346
ST5228	ANTARES / R7081-20	1400	5.62×10^7	6.83×10^5	0.311
ST5228	ANTARES / R7081-20	1500	1.18×10^8	1.25×10^6	0.351
ST5228	ANTARES / R7081-20	1600	2.20×10^8	2.42×10^6	0.348
ST5289	ANTARES / R7081-20	1200	6.61×10^6	1.03×10^5	0.228
ST5289	ANTARES / R7081-20	1300	1.39×10^7	1.85×10^6	0.242
ST5289	ANTARES / R7081-20	1400	3.29×10^7	5.66×10^5	0.173
ST5289	ANTARES / R7081-20	1500	6.62×10^7	1.04×10^6	0.187
ST5311	ANTARES / R7081-20	1300	1.84×10^7	2.64×10^5	0.211
ST5311	ANTARES / R7081-20	1400	3.88×10^7	5.17×10^5	0.262
ST5311	ANTARES / R7081-20	1500	8.10×10^7	1.11×10^6	0.225
ST5311	ANTARES / R7081-20	1600	1.59×10^8	1.84×10^6	0.271
ST5326	ANTARES / R7081-20	1200	4.58×10^6	8.63×10^4	0.145
ST5326	ANTARES / R7081-20	1300	9.28×10^6	2.01×10^5	0.169
ST5326	ANTARES / R7081-20	1400	1.92×10^7	3.55×10^5	0.142
ST5326	ANTARES / R7081-20	1500	3.80×10^7	5.78×10^5	0.148
ST5332	ANTARES / R7081-20	1200	2.07×10^7	2.22×10^5	0.362
ST5332	ANTARES / R7081-20	1300	4.72×10^7	5.98×10^5	0.284
ST5332	ANTARES / R7081-20	1400	1.00×10^8	1.30×10^6	0.303
ST5332	ANTARES / R7081-20	1500	1.95×10^8	2.36×10^6	0.376
ST5403	ANTARES / R7081-20	1200	1.14×10^7	2.32×10^5	0.168
ST5403	ANTARES / R7081-20	1300	2.73×10^7	4.17×10^5	0.174
ST5403	ANTARES / R7081-20	1400	5.29×10^7	1.55×10^6	0.157
ST5403	ANTARES / R7081-20	1500	1.12×10^8	2.07×10^6	0.169

SN	Type/Base	HV [V]	G	σ_G	λ
ST5451	ANTARES / R7081-20	1200	4.15×10^6	9.26×10^4	0.298
ST5451	ANTARES / R7081-20	1300	9.68×10^6	1.40×10^5	0.276
ST5451	ANTARES / R7081-20	1400	1.97×10^7	3.87×10^5	0.287
ST5451	ANTARES / R7081-20	1500	4.04×10^7	5.37×10^5	0.251
ST5484	ANTARES / R7081-20	1200	1.90×10^7	1.89×10^5	0.602
ST5484	ANTARES / R7081-20	1300	4.43×10^7	3.99×10^5	0.617
ST5484	ANTARES / R7081-20	1400	9.05×10^7	8.34×10^5	0.658
ST5484	ANTARES / R7081-20	1500	1.72×10^8	1.91×10^6	0.624
ST5496	ANTARES / R7081-20	1200	1.53×10^7	2.39×10^5	0.219
ST5496	ANTARES / R7081-20	1300	3.33×10^7	5.20×10^5	0.222
ST5496	ANTARES / R7081-20	1400	7.14×10^7	1.09×10^6	0.217
ST5496	ANTARES / R7081-20	1500	1.35×10^8	2.41×10^6	0.219
ST5498	ANTARES / R7081-20	1100	1.19×10^7	1.54×10^5	0.247
ST5498	ANTARES / R7081-20	1200	2.91×10^7	4.37×10^5	0.271
ST5498	ANTARES / R7081-20	1300	6.87×10^7	8.37×10^5	0.290
ST5498	ANTARES / R7081-20	1400	1.40×10^8	1.06×10^7	0.329
ST5564	ANTARES / R7081-20	1200	5.95×10^6	1.31×10^5	0.114
ST5564	ANTARES / R7081-20	1300	1.37×10^7	2.84×10^5	0.131
ST5564	ANTARES / R7081-20	1400	2.93×10^7	4.44×10^5	0.172
ST5564	ANTARES / R7081-20	1500	4.81×10^7	1.07×10^7	0.143
ST5628	ANTARES / R7081-20	1100	2.81×10^6	3.28×10^4	0.461
ST5628	ANTARES / R7081-20	1200	6.37×10^6	1.11×10^5	0.335
ST5628	ANTARES / R7081-20	1300	1.49×10^7	1.72×10^5	0.302
ST5628	ANTARES / R7081-20	1400	2.98×10^7	3.69×10^5	0.361
ST5649	ANTARES / R7081-20	1200	1.23×10^7	1.48×10^5	0.297
ST5649	ANTARES / R7081-20	1300	2.56×10^7	3.38×10^5	0.288
ST5649	ANTARES / R7081-20	1400	5.59×10^7	7.10×10^5	0.296
ST5649	ANTARES / R7081-20	1500	1.10×10^8	1.33×10^6	0.303
ST5649	ANTARES / R7081-20	1600	1.94×10^8	2.94×10^6	0.310
ST5690	ANTARES / R7081-20	1200	2.43×10^7	2.56×10^5	0.828
ST5690	ANTARES / R7081-20	1300	5.58×10^7	5.67×10^5	0.801
ST5690	ANTARES / R7081-20	1400	1.17×10^8	1.20×10^6	0.806
ST5690	ANTARES / R7081-20	1500	2.43×10^8	2.40×10^6	0.724
ST5695	ANTARES / R7081-20	1200	5.16×10^6	5.27×10^4	0.696
ST5695	ANTARES / R7081-20	1300	1.16×10^7	1.05×10^5	0.636
ST5695	ANTARES / R7081-20	1400	2.37×10^7	2.03×10^5	0.726
ST5695	ANTARES / R7081-20	1500	4.77×10^7	4.47×10^5	0.694

SN	Type/Base	HV [V]	G	σ_G	λ
ST5695	ANTARES / R7081-20	1600	8.75×10^7	8.10×10^5	1.222
ST5784	ANTARES / R7081-20	1200	1.91×10^7	4.58×10^5	0.101
ST5784	ANTARES / R7081-20	1300	4.76×10^7	9.81×10^5	0.089
ST5784	ANTARES / R7081-20	1400	9.31×10^7	2.13×10^6	0.109
ST5784	ANTARES / R7081-20	1500	1.82×10^8	4.36×10^6	0.084
ST5810	ANTARES / R7081-20	1200	5.49×10^6	1.20×10^5	0.229
ST5810	ANTARES / R7081-20	1300	1.23×10^7	1.89×10^5	0.255
ST5810	ANTARES / R7081-20	1400	2.76×10^7	3.48×10^5	0.235
ST5810	ANTARES / R7081-20	1500	5.42×10^7	7.72×10^5	0.220
ST5810	ANTARES / R7081-20	1600	9.75×10^7	1.49×10^6	0.211
ST5813	ANTARES / R7081-20	1200	1.10×10^7	2.90×10^5	0.088
ST5813	ANTARES / R7081-20	1300	2.49×10^7	1.01×10^6	0.076
ST5813	ANTARES / R7081-20	1400	5.21×10^7	1.04×10^6	0.109
ST5813	ANTARES / R7081-20	1500	9.76×10^7	2.10×10^6	0.100
ST6003	ANTARES / R7081-20	1200	1.68×10^7	2.45×10^5	0.213
ST6003	ANTARES / R7081-20	1300	3.70×10^7	6.22×10^5	0.180
ST6003	ANTARES / R7081-20	1400	8.31×10^7	1.25×10^6	0.184
ST6003	ANTARES / R7081-20	1500	1.69×10^8	2.23×10^6	0.221
ST6008	ANTARES / R7081-20	1200	2.07×10^7	2.00×10^5	0.485
ST6008	ANTARES / R7081-20	1300	4.62×10^7	7.18×10^5	0.158
ST6008	ANTARES / R7081-20	1400	9.97×10^7	1.53×10^6	0.172
ST6008	ANTARES / R7081-20	1600	3.94×10^8	6.52×10^6	0.145
ST6020	ANTARES / R7081-20	1200	9.05×10^6	1.64×10^5	0.145
ST6020	ANTARES / R7081-20	1300	2.01×10^7	2.83×10^5	0.184
ST6020	ANTARES / R7081-20	1400	4.21×10^7	6.21×10^5	0.146
ST6020	ANTARES / R7081-20	1500	7.92×10^7	1.44×10^6	0.180
ST6023	ANTARES / R7081-20	1200	5.72×10^6	1.31×10^5	0.106
ST6023	ANTARES / R7081-20	1300	1.25×10^7	2.52×10^5	0.139
ST6023	ANTARES / R7081-20	1400	2.68×10^7	5.99×10^5	0.114
ST6023	ANTARES / R7081-20	1500	5.42×10^7	1.24×10^6	0.112
ST6068	ANTARES / R7081-20	1200	1.16×10^7	2.22×10^5	0.249
ST6068	ANTARES / R7081-20	1300	2.62×10^7	4.03×10^5	0.258
ST6068	ANTARES / R7081-20	1400	5.43×10^7	9.37×10^5	0.286
ST6068	ANTARES / R7081-20	1500	1.11×10^8	1.30×10^6	0.269
ST6068	ANTARES / R7081-20	1600	2.13×10^8	2.69×10^6	0.271
ST6198	ANTARES / R7081-20	1200	1.15×10^7	1.54×10^5	0.251
ST6198	ANTARES / R7081-20	1300	2.51×10^7	4.36×10^5	0.248

SN	Type/Base	HV [V]	G	σ_G	λ
ST6198	ANTARES / R7081-20	1400	5.42×10^7	7.37×10^5	0.273
ST6198	ANTARES / R7081-20	1500	1.06×10^8	1.94×10^6	0.230
ST6217	ANTARES / R7081-20	1200	8.08×10^6	1.03×10^5	0.408
ST6217	ANTARES / R7081-20	1300	1.93×10^7	1.96×10^5	0.465
ST6217	ANTARES / R7081-20	1400	4.05×10^7	4.12×10^5	0.397
ST6217	ANTARES / R7081-20	1500	7.92×10^7	7.91×10^5	0.466
ST6228	ANTARES / R7081-20	1200	8.27×10^6	1.41×10^5	0.133
ST6228	ANTARES / R7081-20	1300	1.82×10^7	3.14×10^5	0.130
ST6228	ANTARES / R7081-20	1400	3.77×10^7	6.89×10^5	0.105
ST6228	ANTARES / R7081-20	1500	7.41×10^7	1.24×10^6	0.128
ST6242	ANTARES / R7081-20	1200	4.36×10^7	6.66×10^5	0.210
ST6242	ANTARES / R7081-20	1300	1.06×10^8	1.42×10^6	0.214
ST6242	ANTARES / R7081-20	1400	2.17×10^8	2.89×10^6	0.236
ST6242	ANTARES / R7081-20	1500	4.57×10^8	5.84×10^6	0.231
ST6242	ANTARES / R7081-20	1600	8.87×10^8	1.05×10^7	0.246
ST6256	ANTARES / R7081-20	1200	1.83×10^7	3.48×10^5	0.202
ST6256	ANTARES / R7081-20	1300	4.41×10^7	6.38×10^5	0.112
ST6256	ANTARES / R7081-20	1400	9.15×10^7	1.94×10^6	0.189
ST6256	ANTARES / R7081-20	1500	1.98×10^8	2.72×10^6	0.201
ST6270	ANTARES / R7081-20	1200	5.17×10^6	1.23×10^5	0.089
ST6270	ANTARES / R7081-20	1300	1.11×10^7	2.54×10^5	0.107
ST6270	ANTARES / R7081-20	1400	2.24×10^7	4.94×10^5	0.120
ST6270	ANTARES / R7081-20	1500	4.55×10^7	8.82×10^5	0.125
ST6271	ANTARES / R7081-20	1200	8.32×10^6	1.78×10^5	0.147
ST6271	ANTARES / R7081-20	1300	2.00×10^7	3.36×10^5	0.132
ST6271	ANTARES / R7081-20	1400	4.03×10^7	8.97×10^5	0.157
ST6271	ANTARES / R7081-20	1500	8.42×10^7	1.47×10^6	0.131
ST6277	ANTARES / R7081-20	1200	6.28×10^6	2.11×10^5	0.087
ST6277	ANTARES / R7081-20	1300	1.44×10^7	2.69×10^5	0.165
ST6277	ANTARES / R7081-20	1400	3.07×10^7	5.33×10^5	0.148
ST6277	ANTARES / R7081-20	1500	6.10×10^7	1.34×10^6	0.099
ST6282	ANTARES / R7081-20	1200	1.33×10^7	1.33×10^5	0.514
ST6282	ANTARES / R7081-20	1300	3.12×10^7	1.72×10^6	0.617
ST6282	ANTARES / R7081-20	1400	6.61×10^7	6.19×10^5	0.638
ST6282	ANTARES / R7081-20	1500	1.33×10^8	1.25×10^6	0.580
ST6300	ANTARES / R7081-20	1200	2.12×10^7	2.09×10^5	0.411
ST6300	ANTARES / R7081-20	1300	4.95×10^7	4.65×10^5	0.413

SN	Type/Base	HV [V]	G	σ_G	λ
ST6300	ANTARES / R7081-20	1400	1.03×10^8	9.81×10^5	0.464
ST6300	ANTARES / R7081-20	1500	2.07×10^8	1.29×10^6	0.505
ST6300	ANTARES / R7081-20	1600	3.91×10^8	3.64×10^6	0.470
ST6304	ANTARES / R7081-20	1200	1.53×10^7	2.80×10^5	0.158
ST6304	ANTARES / R7081-20	1300	3.54×10^7	5.63×10^5	0.149
ST6304	ANTARES / R7081-20	1400	7.27×10^7	1.14×10^6	0.208
ST6304	ANTARES / R7081-20	1500	1.49×10^8	2.45×10^6	0.131
ST6304	ANTARES / R7081-20	1600	2.91×10^8	5.99×10^6	0.102
ST6327	ANTARES / R7081-20	1200	1.31×10^7	3.13×10^5	0.195
ST6327	ANTARES / R7081-20	1300	3.14×10^7	5.26×10^5	0.183
ST6327	ANTARES / R7081-20	1400	6.97×10^7	9.35×10^5	0.206
ST6327	ANTARES / R7081-20	1500	1.40×10^8	1.95×10^6	0.182
ST6331	ANTARES / R7081-20	1200	1.52×10^7	2.02×10^5	0.448
ST6331	ANTARES / R7081-20	1300	3.64×10^7	4.09×10^5	0.349
ST6331	ANTARES / R7081-20	1400	7.55×10^7	8.96×10^5	0.377
ST6331	ANTARES / R7081-20	1500	1.50×10^8	1.89×10^6	0.397
ST6345	ANTARES / R7081-20	1200	1.65×10^7	1.55×10^5	0.669
ST6345	ANTARES / R7081-20	1300	3.74×10^7	4.49×10^5	0.662
ST6345	ANTARES / R7081-20	1400	8.75×10^7	6.23×10^6	0.742
ST6345	ANTARES / R7081-20	1500	1.70×10^8	1.55×10^6	0.626
ST6352	ANTARES / R7081-20	1200	5.73×10^6	9.66×10^4	0.133
ST6352	ANTARES / R7081-20	1300	1.26×10^7	1.93×10^5	0.155
ST6352	ANTARES / R7081-20	1400	2.42×10^7	5.26×10^5	0.111
ST6352	ANTARES / R7081-20	1500	5.04×10^7	8.71×10^5	0.151
TM0007	Reference / R7081-20	1200	1.57×10^8	1.52×10^6	0.424
TM0007	Reference / R7081-20	1300	3.76×10^8	3.55×10^6	0.448
TM0007	Reference / R7081-20	1400	8.52×10^8	8.81×10^6	0.409
TM0007	Reference / R7081-20	1500	1.84×10^9	1.82×10^7	0.389
TM0007	Reference / R7081-20	1600	4.00×10^9	3.98×10^7	0.420

Table A.2: Complete list of HV_{nom} at $G = 5 \times 10^7$ for all ANTARES PMTs, with propagated 1σ uncertainty.

Serial	HV_{nom} [V]	$\sigma(HV_{\text{nom}})$ [V]
ST5228	1383	3
ST5289	1459	2
ST5311	1432	3

Serial	HV_{nom} [V]	$\sigma(HV_{\text{nom}})$ [V]
ST5326	1546	4
ST5332	1318	5
ST5403	1368	4
ST5451	1532	3
ST5484	1269	3
ST5496	1372	3
ST5498	1263	3
ST5564	1448	4
ST5628	1474	3
ST5649	1385	4
ST5690	1259	2
ST5695	1323	4
ST5784	1366	2
ST5810	1434	4
ST5813	1442	3
ST6003	1334	4
ST6008	1209	3
ST6020	1474	4
ST6023	1478	4
ST6068	1423	4
ST6198	1390	2
ST6217	1496	5
ST6228	1350	3
ST6242	1214	4
ST6256	1358	3
ST6270	1498	4
ST6271	1467	4
ST6277	1470	2
ST6282	1357	5
ST6300	1295	5
ST6304	1387	4
ST6327	1417	4
ST6331	1381	3
ST6345	1334	2
ST6352	1501	4
TM0007	1083	1

B Git repository for scripts

All analysis and utility scripts developed for this thesis are hosted in a public Git repository:

`https://github.com/kavan-purohit/
Gain-Characterisation-of-ANTARES-PMTs-for-SWGO`

List of Figures

- Figure 1.1: All-particle cosmic-ray energy spectrum compiled from multiple air-shower experiments, showing the characteristic features known as the “knee” and the “ankle”. Data from HEGRA, CASA-MIA, KASCADE, IceTop, Tunka, HiRes, Telescope Array, and Auger are shown for comparison. Adapted from Gaisser and Stanev [9]. 3
- Figure 1.2: Schematic representation of an extensive air shower showing its hadronic, electromagnetic, and muonic components. Adapted from Pawlicki [23]. 3
- Figure 1.3: Global distribution of major ground-based gamma-ray observatories. Current facilities are shown in green, planned or future observatories in blue, and past experiments in red. The planned SWGO site in South America will provide wide-field coverage of the southern sky. Figure adapted from [29] 4
- Figure 1.4: Sky visibility of the Southern Wide-field Gamma-ray Observatory (SWGO). The colored band represents the Galactic Plane and the regions visible to SWGO above 45° and 60° elevation from its planned southern-hemisphere site. Adapted from Abreu *et al.* [3]. 6
- Figure 1.5: Schematic view of a water-Cherenkov detector (WCD) unit designed for the Southern Wide-field Gamma-ray Observatory (SWGO). The cylindrical tank contains two PMTs mounted vertically—one facing upward and one facing downward—to enable muon tagging and gamma–hadron discrimination. Adapted from Leitl [18]. 7

Figure 1.6:	Planned SWGO-A layout showing seven detector clusters, each consisting of 55 water-Cherenkov detectors (WCDs) and a central field node (blue rectangle). This configuration forms the prototype subarray of the full SWGO design. Adapted from Abreu <i>et al.</i> [3].	8
Figure 1.7:	Schematic view of the ANTARES neutrino telescope in the Mediterranean Sea, showing the arrangement of the detection lines with storeys and optical modules, the sea-bed junction box, and the 40 km cable connecting the detector to the onshore station. Adapted from Zornoza and Zúñiga [7].	10
Figure 1.8:	Schematic view of a single ANTARES optical module (OM), showing the internal components including the 10-inch Hamamatsu R7081-20 PMT, optical gel, magnetic shield, LED calibration device, and the pressure-resistant glass sphere. Adapted from Zornoza and Zúñiga [7].	11
Figure 2.1:	Schematic views of (a) an electromagnetic cascade and (b) a hadronic shower. In the hadronic cascade, dashed lines indicate neutral pions that decay rapidly into photons, generating electromagnetic sub-showers. The diagrams illustrate the multiplicative nature of shower development as described by the Heitler–Matthews model. Adapted from Matthews [20].	14
Figure 2.2:	Simulated depth of shower maximum X_{\max} versus calorimetric energy E_{cal} for proton (red) and iron (blue) primaries using three hadronic-interaction models: EPOS 1.99, Sibyll 2.1, and QGSJetII-03. The separation of the distributions illustrates the sensitivity of X_{\max} to the primary mass and to the relative contributions of electromagnetic and hadronic components in shower development. Adapted from Kampert and Unger [15].	16
Figure 2.3:	Schematic representation of Cherenkov radiation showing the characteristic light cone emitted by a charged particle moving faster than the phase velocity of light in a dielectric medium. The opening angle θ_c satisfies $\cos \theta_c = 1/(\beta n)$. Adapted from Alaeian [4].	18

Figure 2.4: Schematic illustration of Cherenkov light production and detection in a water-Cherenkov detector (WCD). A relativistic charged particle from an extensive air shower passes through the water volume, emitting Cherenkov photons at an angle θ_c with respect to its trajectory. The light front reaches the PMTs mounted at the bottom, where the resulting photoelectrons are amplified to produce measurable signals. Adapted from Abreu *et al.* [3]. 19

Figure 2.5: Schematic representation of a PMT showing the photocathode, focusing electrodes, dynode chain, and anode. Incident photons release photoelectrons at the photocathode, which are accelerated toward the first dynode, generating secondary electrons that are successively multiplied and collected at the anode. Adapted from Hamamatsu Photonics [24]. 21

Figure 2.6: Simplified base-circuit schematic of the Hamamatsu R7081-20 PMT. The high-voltage divider network distributes the bias across 14 dynode stages and focusing electrodes, while capacitors stabilize the potential differences to ensure gain linearity and timing stability. The signal output is coupled capacitively to the readout electronics. Redrawn taking inspiration from [14, 17]. 22

Figure 2.7: Measured gain–voltage relation for the ANTARES PMT ST5498. The logarithmic fit illustrates the expected power-law dependence, $G \propto V^\kappa$, where κ is obtained from the slope of the fitted line. In this case, the value of $\kappa \approx 8.5$ 23

Figure 2.8: Single-photoelectron charge spectrum with a clearly separated SPE peak. 24

Figure 2.9: Quantum efficiency and photocathode radiant sensitivity of the Hamamatsu R7081-20 PMT as a function of wavelength. The bialkali photocathode exhibits peak sensitivity in the blue region near 400 nm. Adapted from Hamamatsu Photonics [10]. 25

Figure 3.1: Dark room with the light-tight measurement box. Cables are routed via feedthroughs. 28

Figure 3.2:	Light-tight measurement setup: (a) with the dark box closed and (b) with the dark box open, showing the PMT placed inside.	28
Figure 3.3:	Whole instrument setup in the lab.	29
Figure 3.4:	iseg SHR high-voltage supply used for PMT biasing. . . .	30
Figure 3.5:	(a) Signal pick-off device for HV and signal routing, and (b) 14-pin socket adapter interfacing the 10" PMT.	30
Figure 3.6:	Signal generation: Rigol DG1022 gating the Alphalas PLDD-50MHV pulsed driver.	31
Figure 3.7:	Representative PMT pulse on the MSO54 together with the acquisition settings visible in a window at bottom (6.25 GS/s, 200 ns, 20 ns/div). The displayed pulse is generated from one of the ANTARES PMTs.	32
Figure 3.8:	(a) ANTARES PMTs inside their original optical modules (OMs) prior to extraction, each containing a 10" PMT enclosed within a glass sphere and (b) the same PMTs after extraction, prepared for gain testing. Adapted from [21]	35
Figure 4.1:	Charge spectrum at a representative HV point. Green — baseline-subtracted histogram of integrated charge Q (logarithmic y -axis). Red — parametric response fit (pedestal + SPE + higher n -pe components). Blue vertical line — automatically determined valley Q_{val} used as a guard rail for the fit and for the P/V diagnostic.	40
Figure 5.1:	Histogram of HV scan points per PMT.	43
Figure 5.2:	SPE occupancy λ vs. HV across all PMTs. Dots show per-PMT, per-HV λ values; the solid line is the median at each HV, and the shaded band indicates the interquartile range (IQR). The near-flat median is consistent with stable illumination and operation in the SPE regime.	44
Figure 5.3:	Charge spectrum at 1400V for PMT ST6198 with the fitted response overlaid. Fit diagnostics are reported in the text.	46
Figure 5.4:	Calibration of $\log_{10} G$ versus $\log_{10} HV$ for PMT ST6198. The best-fit slope κ and the derived HV_{nom} at $G = 5 \times 10^7$ (vertical line).	46

Figure 5.5:	Charge spectrum at 1400V for PMT ST6242 with the fitted response overlaid.	47
Figure 5.6:	Calibration of $\log_{10} G$ versus $\log_{10} HV$ for PMT ST6242 with the derived HV_{nom} at $G = 5 \times 10^7$ (vertical line). . .	47
Figure 5.7:	Charge spectrum at 1400V for PMT ST5326 (edge case) with the fitted response overlaid.	48
Figure 5.8:	Calibration of $\log_{10} G$ versus $\log_{10} HV$ for PMT ST5326 with the derived HV_{nom} at $G = 5 \times 10^7$ (vertical line). . .	48
Figure 5.9:	Distribution of fitted slopes κ for all ANTARES PMTs. The central tendency and spread quantify the uniformity of the gain–HV scaling.	49
Figure 5.10:	Distribution of HV_{nom} at $G = 5 \times 10^7$ for ANTARES PMTs. Entries correspond to the nominal voltages derived from each PMT’s gain–HV calibration.	50
Figure 5.11:	HV_{nom} versus κ for ANTARES PMTs. Each point corresponds to one PMT; a weak or null trend is expected once uncertainties are accounted for.	50
Figure 5.12:	Charge spectrum at 1400V for the reference PMT TM0007 with the fitted response overlaid.	51
Figure 5.13:	Calibration of $\log_{10} G$ versus $\log_{10} HV$ for the reference PMT TM0007 with the derived HV_{nom} at $G = 5 \times 10^7$ (vertical line).	52
Figure 5.14:	Fitted slope κ across ANTARES PMTs (histogram) with the sample median (orange) and interquartile range (IQR, blue band). The reference PMT TM0007 is marked in green at its κ value.	53
Figure 5.15:	Distribution of HV_{nom} at $G = 5 \times 10^7$ for ANTARES PMTs (histogram) with the sample median (orange) and IQR (blue band). The reference PMT TM0007 is marked in green at its HV_{nom}	53
Figure 5.16:	Empirical CDF of HV_{nom} for ANTARES PMTs at $G = 5 \times 10^7$. The dashed line marks the median; the shaded band shows the interquartile range (IQR, 25–75%). The orange point illustrates a high-percentile operating voltage (near the 90th percentile).	54

List of Tables

Table 1.1: Milestones of the SWGO R&D phase, together with completion dates for milestones already completed [3].	9
Table 2.1: Main parameters of the Hamamatsu R7081-20 PMT [25, 22, 17].	26
Table 5.1: PMT inventory: The HV count including the reference PMT. Full per-HV metadata is provided in Appendix A.1.	45
Table 5.2: Reference (TM0007) vs. ANTARES median at $G = 5 \times 10^7$	53
Table 5.3: Final HV_{nom} per selected ANTARES PMTs as well as reference PMT, with propagated 1σ uncertainty. Rows include ST6198 (typical), ST6242 (best), ST5326 (edge), plus informative extremes and a near-median entry. The full fleet appears in Appendix A.	55
Table A.1: HV metadata with serial numbers (SN), type/base, HV set-point, fitted gain (G), its uncertainty (σ_G), and SPE occupancy λ . Only HV groups passing the quality selection are listed.	63
Table A.2: Complete list of HV_{nom} at $G = 5 \times 10^7$ for all ANTARES PMTs, with propagated 1σ uncertainty.	67

Declaration of Originality

I, Kavan Harshal Purohit, student registration number: 23162718, hereby confirm that I completed the submitted work independently and without the unauthorized assistance of third parties and without the use of undisclosed and, in particular, unauthorized aids. This work has not been previously submitted in its current form or in a similar form to any other examination authorities and has not been accepted as part of an examination by any other examination authority.

Where the wording has been taken from other people's work or ideas, this has been properly acknowledged and referenced. This also applies to drawings, sketches, diagrams and sources from the Internet.

In particular, I am aware that the use of artificial intelligence is forbidden unless its use as an aid has been expressly permitted by the examiner. This applies in particular to chatbots (especially ChatGPT) and such programs in general that can complete the tasks of the examination or parts thereof on my behalf.

Any infringements of the above rules constitute fraud or attempted fraud and shall lead to the examination being graded "fail" ("nicht bestanden").

Place, Date

Signature

Acknowledgments

I would like to express my heartfelt gratitude to my supervisor, Dr. Alison Mitchell, for the incredible opportunity to work on this thesis under her guidance. Her unwavering support and encouragement throughout this journey have been invaluable, and her mentorship has played a crucial role in my development within this field.

I am also deeply thankful to Dr. Oleg Kalekin for his expert guidance on the instrumental and physical aspects of my research. His patience and dedication in explaining complex concepts have greatly enhanced my understanding and progress.

Additionally, I would like to extend my appreciation to Saujanya, Sayak, and all my colleagues from the SWGO group and ECAP for their support throughout this journey. A special thank you goes to Frederik for sharing his initial instrumentation scripts from his similar work, which were instrumental in my research.

Finally, I would like to express my deepest gratitude to my loving wife, Mansi, my parents, and my brother for their unwavering support and encouragement. Their presence has been a source of strength for me throughout this process.